European Journal of Medicinal Chemistry 298 (2025) 118039

Contents lists available at ScienceDirect

European Journal of Medicinal Chemistry

journal homepage: www.elsevier.com/locate/ejmech

Research paper

CD44-targeted *N*-benzyltetrahydroisoquinoline derivatives as anticancer agents with high tumor-to-normal cell selectivity

Soledad Romero-Tamudo [a,b,c], M. Dora Carrión [a,c], Meriem Chayah [a,b,c,d], Jose M. Espejo-Román [a,b,c], Carmen Domene [d], Rosario M. Sánchez-Martín [a,b,c], Olga Cruz-López [a,c,*], Ana Conejo-García [a,c,**]

[a] Department of Medicinal and Organic Chemistry and Excellence Research Unit of Chemistry Applied to Biomedicine and the Environment, Faculty of Pharmacy, University of Granada, Campus Cartuja s/n, 18071, Granada, Spain
[b] GENYO, Centre for Genomics and Oncological Research, Pfizer/University of Granada/Andalusian Regional Government, PTS Granada, Avda. Ilustración 114, 18016, Granada, Spain
[c] Instituto de Investigación Biosanitaria ibs.GRANADA, 18012, Granada, Spain
[d] Department of Chemistry, University of Bath, Claverton Down, BA2 7AY, Bath, United Kingdom

ARTICLE INFO

Keywords:
Hyaluronic acid
Cluster of differentiation 44
Tetrahydroisoquinoline
Molecular dynamics simulations
Antiproliferative effect

ABSTRACT

CD44, a cell surface glycoprotein, plays a crucial role in cancer progression by enhancing cell proliferation and resistance to apoptosis. Targeting CD44 with small molecules is a promising cancer therapy strategy. Building on our previous work with the tetrahydroisoquinoline (THIQ) derivative **SRT1**, we designed and synthesized a series of analogues (**SRT2-SRT10**) to explore their anticancer potential. Among these, the sulfonate esters **SRT5** and **SRT6** were the most promising in $CD44^+$ MDA-MB-231 breast cancer cells. They effectively inhibited the HA-CD44 interaction, as demonstrated by binding assays and cell viability studies. In addition, molecular dynamics simulations predict that these esters interact with the same key residues within the CD44-HABD domain as those involved in HA recognition. In $CD44^+$ lung cancer cell lines (A549 and NCI–H23), **SRT1** exhibited the strongest antiproliferative activity (EC_{50} = 0.88 and 0.42 μM, respectively), while **SRT5** and **SRT6** also showed significant efficacy, particularly in NCI–H23 cells. Interestingly, only **SRT1** induced apoptosis, suggesting distinct mechanisms of cell death. Kinase profiling revealed that **SRT5** and **SRT6** inhibited CD44-associated kinases, particularly SRC, contributing to their anticancer effects. In contrast, **SRT1** appeared to act through a kinase-independent pathway. All compounds displayed high selectivity for cancer cells over non-tumoral lung cells. ADME predictions suggested favorable pharmacokinetic properties. Overall, our results underscore the potential of *N*-benzylTHIQ derivatives, as selective agents for targeted therapy of lung cancer and support further *in vivo* validation and mechanistic investigations.

1. Introduction

Cancer remains a major global health challenge, with millions of new cases and deaths reported each year. Among the most prevalent malignancies, breast and lung cancers are particularly significant. In 2022, breast cancer accounted for 2.3 million new cases and 670,000 deaths, making it the leading cancer among women. Lung cancer, the most commonly diagnosed cancer worldwide, also remained the leading cause of cancer-related mortality, with 2.5 million new cases and 1.8 million deaths. These statistics underscore the urgent need for innovative therapeutic strategies and improved access to cancer care [1].

The cluster of differentiation 44 (CD44) is a transmembrane

Abbreviations: HA, hyaluronic acid; CD44, cluster of differentiation 44; CD44-HABD, CD44 HA binding domain; THIQ, tetrahydroisoquinoline; MD, molecular dynamics; SI, selectivity index; BBB, blood brain barrier.

* Corresponding author. Department of Medicinal and Organic Chemistry and Excellence Research Unit of Chemistry Applied to Biomedicine and the Environment, Faculty of Pharmacy, University of Granada, Campus Cartuja s/n, 18071, Granada, Spain.

** Corresponding author. Department of Medicinal and Organic Chemistry and Excellence Research Unit of Chemistry Applied to Biomedicine and the Environment, Faculty of Pharmacy, University of Granada, Campus Cartuja s/n, 18071, Granada, Spain.

E-mail addresses: soledadromero@ugr.es (S. Romero-Tamudo), dcarrion@ugr.es (M.D. Carrión), chayahm@ugr.es (M. Chayah), jmespejo@ugr.es (J.M. Espejo-Román), mcdn20@bath.ac.uk (C. Domene), rmsanchez@ugr.es (R.M. Sánchez-Martín), olgacl@ugr.es (O. Cruz-López), aconejo@ugr.es (A. Conejo-García).

https://doi.org/10.1016/j.ejmech.2025.118039
Received 11 June 2025; Received in revised form 22 July 2025; Accepted 30 July 2025
Available online 5 August 2025

glycoprotein that plays a pivotal role in the progression of several cancers. Upon binding to hyaluronic acid (HA), CD44 undergoes conformational changes that promote the recruitment of adaptor proteins and initiate multiple signalling cascades. Overexpression of CD44 is common in various tumour types and is associated with increased malignancy and poor clinical outcomes. Recent studies have demonstrated that CD44 is significantly overexpressed in the mesenchymal subtype of triple-negative breast cancer cell lines, and it has been associated with enhanced invasive capacity and metastatic potential underscoring the functional role of CD44 in breast tumor progression [2]. CD44 also plays a critical role in lung cancer progression by promoting tumor cell proliferation, migration, and metastasis, and is increasingly recognized as a potential therapeutic target and biomarker in non-small cell lung cancer [3].

HA interacts with CD44 in a multivalent manner, stabilising signalling domains at the plasma membrane. This interaction facilitates the association of CD44 with several key signalling receptors, including ErbB2, EGFR, and c-Met receptor tyrosine kinases; TGF-β receptors; and non-receptor kinases such as members of the Src and Ras families (Fig. 1). These interactions activate oncogenic pathways such as MAPK/ERK, PI3K/AKT, and FAK, driving cancer cell proliferation, adhesion, survival, motility, invasion, chemoresistance, angiogenesis, and metabolic reprogramming [4],[5].

Due to its involvement in multiple signaling pathways, CD44 is considered both a prognostic marker and therapeutic target. Various strategies are under investigation for CD44-targeted therapy, including monoclonal antibodies [6], [7], glycolipids extracted from fungi [8],[9], or oligosaccharides that mimic HA [10–12], particularly in cancers with high CD44 expression.

Structural studies using X-ray crystallography and NMR have elucidated the structure of CD44, particularly its HA-binding domain (HABD) located in the extracellular N-terminal region [13], [14]. Fragment screening and binding assays have revealed an inducible pocket near the HA-binding site, opening opportunities for small-molecule targeting [15]. Although THIQ derivatives have emerged as lead compounds, their reported binding affinities were in the low millimolar range, and their anticancer activity had not yet been evaluated. [15]

Our research group previously developed a series of *N*-aryl and *N*-alkyl THIQ derivatives (Fig. 2) designed to interact with CD44 [16-18]. Computational studies indicated that these compounds bind to CD44-HABD in a manner consistent with reported crystal structures. [15] These findings were supported by fluorescence-based competitive binding assays in the $CD44^+$ breast cancer cell line MDA-MB-231. The lead compound, **SRT1**, exhibited an EC_{50} of 0.59 μM in MDA-MB-231 cells, disrupted cancer spheroid integrity, and reduced cell viability in a dose-dependent manner. [17]

In the present study, we expand on our earlier work by synthesizing and evaluating a series of new THIQ derivatives (**SRT2**–**SRT10**). We assessed their antiproliferative activity in $CD44^+$ breast and lung cancer cell lines (MDA-MB-231, A549, and NCI–H23). Molecular docking, molecular dynamics simulations, and competitive binding assays were employed to characterise interactions with CD44-HABD. Additionally, we performed apoptosis assays, selectivity index (SI) evaluations, and kinase inhibition studies to investigate the underlying mechanisms of action.

2. Result and discussion

2.1. Design

The design of compounds **SRT2** to **SRT10** was guided by the structural features of the lead compound **SRT1**. This compound comprises a 5-hydroxyTHIQ core bearing a 3,4,5-trimethoxybenzyl substituent at position 2 (Fig. 2 and Table 1). Compounds **SRT2**-**SRT4** preserve the hydroxyl group on the THIQ core to ensure potential anchoring to the previously described THIQ binding site, but they include modifications on the trimethoxybenzyl ring to investigate interactions in the regions surrounding this pocket. In a different approach, compounds **SRT5**-**SRT10** introduce sulfonate ester moieties to extend the scaffold into the adjacent HA-binding groove of CD44. This enables deeper engagement

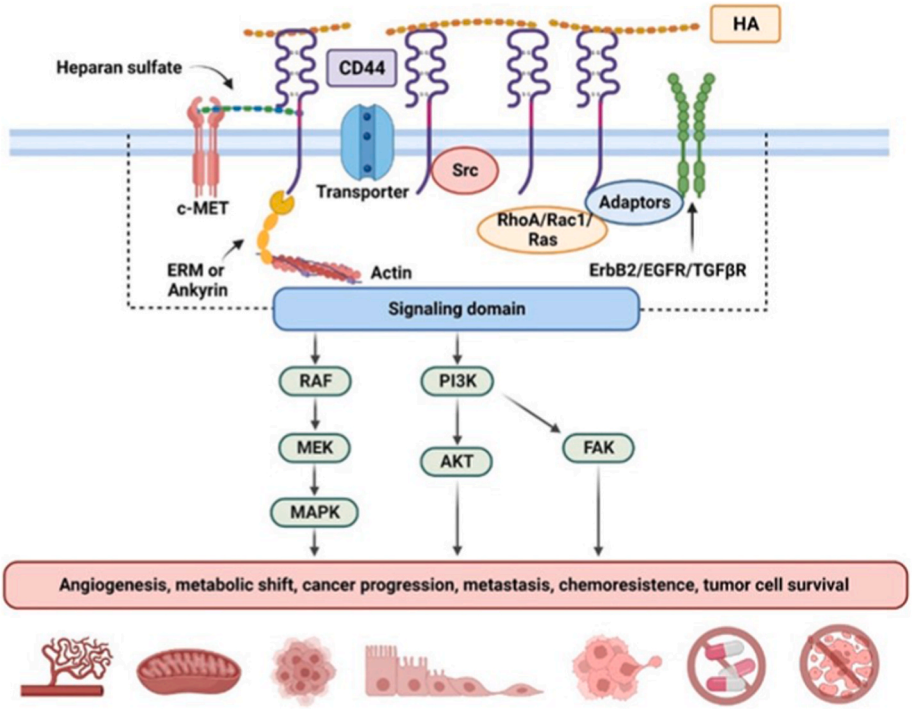

Fig. 1. HA-CD44 interaction activates multiple intracellular signaling pathways, including those involving protein kinases, cytoskeletal changes and transcription factors. These cascades contribute to key pathological processes such as angiogenesis, metabolic changes, tumor cell adhesion, proliferation, migration, metastasis, drug resistance and evasion from apoptosis.

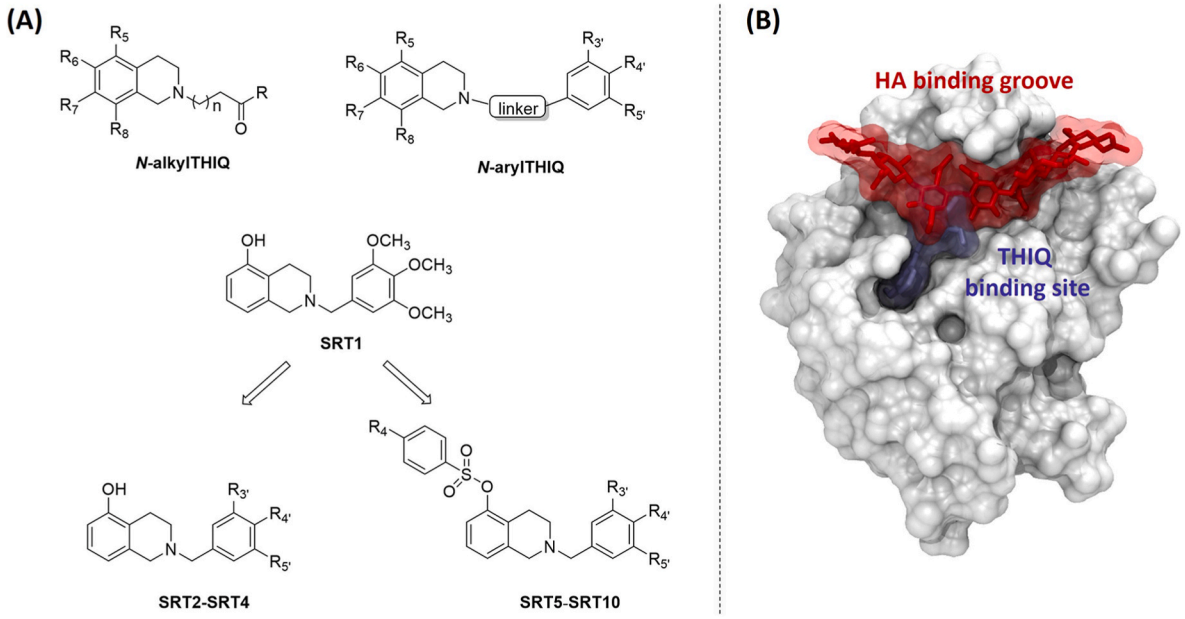

Fig. 2. A) Chemical structures of previously reported compounds, including the lead **SRT1** and the newly designed targets **SRT2-SRT10. B)** The crystallographic structure of CD44-HABD (PDB ID: 5BZK) in grey highlighting the localization of HA (PDB ID: 2JCR) in red and the compound **SRT1** docked structure in ice blue. (For interpretation of the references to colour in this figure legend, the reader is referred to the Web version of this article.)

with residues involved in HA recognition. Thus, in **SRT2-SRT4**, modifications were limited to the R3′, R4′ and R5′ methoxy groups: **SRT2** lacks the OCH_3 group at R4′ while **SRT3** and **SRT4** feature electron-withdrawing substituents at this position CF_3 and NO_2, respectively and sulfonylated derivatives (**SRT5-SRT10**) incorporate either CH_3 or NO_2 groups in para position.

To validate our design strategy and assess the binding potential of the new compounds to the CD44 binding site, molecular docking studies were performed. Specifically, we evaluated the binding affinity and interaction profiles of **SRT2** to **SRT10** within the CD44-HABD. The previously reported compound **SRT1** was included as a reference.

Fig. 3 presents the docking poses of compounds **SRT1-SRT4** and **SRT5-SRT10**. The poses are consistent with those observed in our earlier work [17]. All compounds demonstrated strong predicted binding affinities for CD44, engaging key residues within the THIQ binding pocket and adjacent sites.

Compounds **SRT2-SRT10** exhibit interactions primarily with residues Arg155, Asn154, Val153, Thr31, Val30, Asn29, Glu41, and Arg82 within the THIQ binding site of CD44-HABD. Notably, the sulfonate esters **SRT5-SRT10** extend further into the HA binding groove, forming additional interactions with residues located deeper in the pocket, such as Asp98 and His96.

SRT2-SRT4 tend to form more specific interactions through the THIQ moiety, particularly with Arg155 and Asn154, which may contribute to binding specificity, as previously observed for **SRT1**. In contrast, **SRT5-SRT10** demonstrate broader interaction profiles, engaging not only Arg82 and Cys81 but also Thr80, Asp98, and His96. This suggests a more versatile binding mode, potentially enhancing the compounds' stability and efficacy. The interactions observed in this docking study support the potential of these compounds to stably bind within the CD44 HA binding domain.

Table 1
Antiproliferative activities of the synthesized compounds **SRT1** to **SRT10** against MDA-MB-231, A549 and NCl–H23 cells.

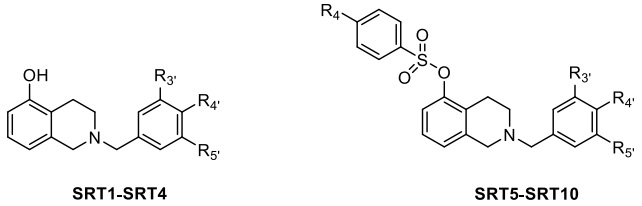

Compounds	$R_{3'}$	$R_{4'}$	$R_{5'}$	R_4	EC_{50} (μM) MDA-MB-231	EC_{50} (μM) A549	EC_{50} (μM) NCI–H23
SRT1	OCH_3	OCH_3	OCH_3	–	0.93 ± 0.08	0.88 ± 0.31	0.42 ± 0.07
SRT2	OCH_3	H	OCH_3	–	8.98 ± 1.20	13.09 ± 1.80	16.79 ± 2.49
SRT3	H	CF_3	H	–	33.74 ± 12.81	20.20 ± 1.23	23.46 ± 1.26
SRT4	H	NO_2	H	–	>100	>100	28.31 ± 10.85
SRT5	OCH_3	OCH_3	OCH_3	CH_3	10.13 ± 1.88	4.05 ± 1.36	3.11 ± 1.83
SRT6	OCH_3	OCH_3	OCH_3	NO_2	7.57 ± 1.20	5.00 ± 0.83	1.37 ± 0.52
SRT7	OCH_3	H	OCH_3	CH_3	49.02 ± 25.60	40.33 ± 9.67	3.14 ± 0.86
SRT8	OCH_3	H	OCH_3	NO_2	24.24 ± 14.74	33.14 ± 2.64	4.80 ± 1.97
SRT9	H	CF_3	H	CH_3	48.89 ± 1.63	39.14 ± 10.86	4.00 ± 1.28
SRT10	H	CF_3	H	NO_2	10.44 ± 0.45	8.82 ± 1.82	2.33 ± 0.41

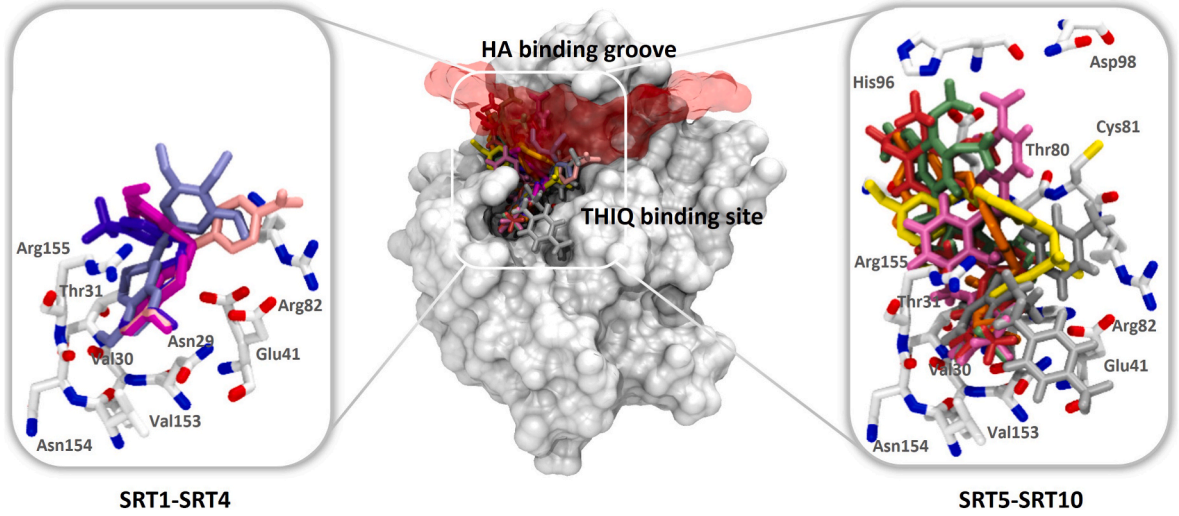

Fig. 3. Molecular docking of compounds **SRT1-SRT10** in the THIQ binding site, near the HA binding groove of CD44-HABD (PDB ID: 5BZK, depicted in grey). HA (PDB ID: 2JCR) is shown in red transparent surface. Compound **SRT1** is represented in ice blue, **SRT2** in magenta, **SRT3** in violet, **SRT4** in pink, **SRT5** in red, **SRT6** in green, **SRT7** in yellow, **SRT8** in orange, **SRT9** in silver and **SRT10** in mauve. (For interpretation of the references to colour in this figure legend, the reader is referred to the Web version of this article.)

2.2. Chemical synthesis

The synthesis of target compounds **SRT1-SRT10** is outlined in Scheme 1. The key intermediate, 1,2,3,4-tetrahydroisoquinolin-5-ol acetate, was prepared by the reduction of isoquinolin-5-ol (step i, Scheme 1) as previously described. [17] Nucleophilic substitution of the corresponding benzyl halides - 3,5-dimethoxybenzyl bromide, 3,4,5-trimethoxybenzylchloride benzyl chloride, 4-(trifluoromethyl) benzyl bromide or 4-nitrobenzyl bromide - with the intermediate in the presence of Et_3N in absolute ethanol yielded compounds **SRT1-SRT4** (step ii, Scheme 1). These reactions proceeded with moderate yields (20–69 %). The sulfonate ester derivatives (**SRT5-SRT10**) were subsequently obtained by reacting the corresponding alcohols with either 4-methyl- or 4-nitrobenzenesulfonyl chloride in absolute ethanol, using Et_3N as a base (step iii, Scheme 1). These reactions afforded the desired products with average yields of 62 %.

2.3. Antiproliferative activity in MDA-MB-231 breast cancer cells

The $CD44^+$ human MDA-MB-231 breast adenocarcinoma cell line was selected for this study. CD44 overexpression was confirmed *via* flow cytometry using the anti-CD44 antibody IM7, validating the suitability of the cell line for evaluating the cytotoxic effects of HA-CD44 inhibitors (Fig. S1). The antiproliferative activity of compounds **SRT2-SRT10** was assessed by determining the half maximal effective concentration (EC_{50}) *in vitro* assays with MDA-MB-231 cells (Table 1), with **SRT1** included as a reference compound. Cell viability was measured using a fluorescent resazurin assay, and EC_{50} values were calculated from 10-point semilog dose-response curves (Table 1, Fig. 4 and Figs. S2–S4). Initially, MDA-MB-231 cells were exposed to increasing concentrations of the compounds (ranging from 0.001 to 100 μM) over a 120-h period to establish the inhibitor dose range necessary for assessing antiproliferative activity.

The evaluation of the antiproliferative activity of the target compound against the MDA-MB-231 cell line revealed significant differences depending on the structural modifications introduced.

Compound **SRT1** exhibited the highest activity with an EC_{50} of 0.93 μM, consistent with our previously reported data. [17] Derivatives **SRT2**, **SRT3** and **SRT4**, which feature modifications only at positions $R_{3'}$, $R_{4'}$ and $R_{5'}$, showed a significant decrease in activity, with EC_{50} values of 8.98, 33.74 and > 100 μM respectively.

In particular, the removal of the OCH_3 at this position $R_{4'}$ in **SRT2** appears to be unfavorable for activity, suggesting that the presence of a OCH_3 group at this position is important for interaction with the biological binding site. Compounds **SRT3** and **SRT4**, which lack three OCH_3 and contain CF_3 and NO_2 groups at $R_{4'}$, respectively, exhibited a drastic reduction in activity likely due to electron-withdrawing effects that reduce target binding affinity.

All experiments were performed in triplicate, and similar results were obtained in each case. Data are presented as mean ± SEM from three independent experiments.

Incorporation of the sulfonate ester moiety (**SRT5-SRT10**) generally led to a decrease in activity, except for **SRT10**. As **SRT4** showed no activity, its corresponding esters were not synthesized. Among the esters, a similar trend to that observed for **SRT1** to **SRT3** was evident. The presence of three OCH_3 groups at positions $R_{3'}$, $R_{4'}$, and $R_{5'}$ (**SRT5** and **SRT6**) resulted in the most active compounds, with EC_{50} values of 10.13 and 7.57 μM, respectively (Fig. 4). In contrast, the removal of the OCH_3 group at position $R_{4'}$ led to a decrease in activity, with **SRT7** and **SRT8** exhibiting significantly lower activity (EC_{50} values of 49.02 and 24.24

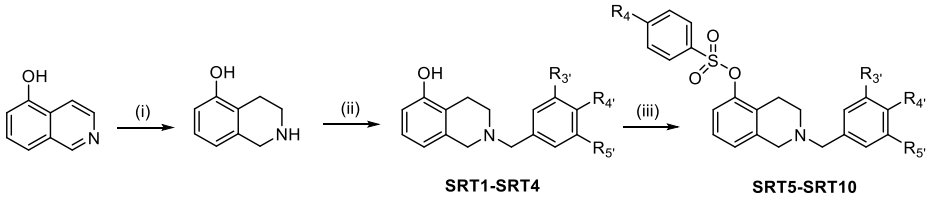

Scheme 1. *Reagents and conditions:* (i) H_2, PtO_2, AcOH, H_2SO_4 96 %, 55 psi, 24 h, rt; (ii) Et_3N, EtOH, rt 1h, benzyl halide, Et_3N, 0 °C 10 min, rt overnight; (iii) Et_3N, EtOH, aryl sulfonyl chloride, 0 °C 10 min, rt overnight.

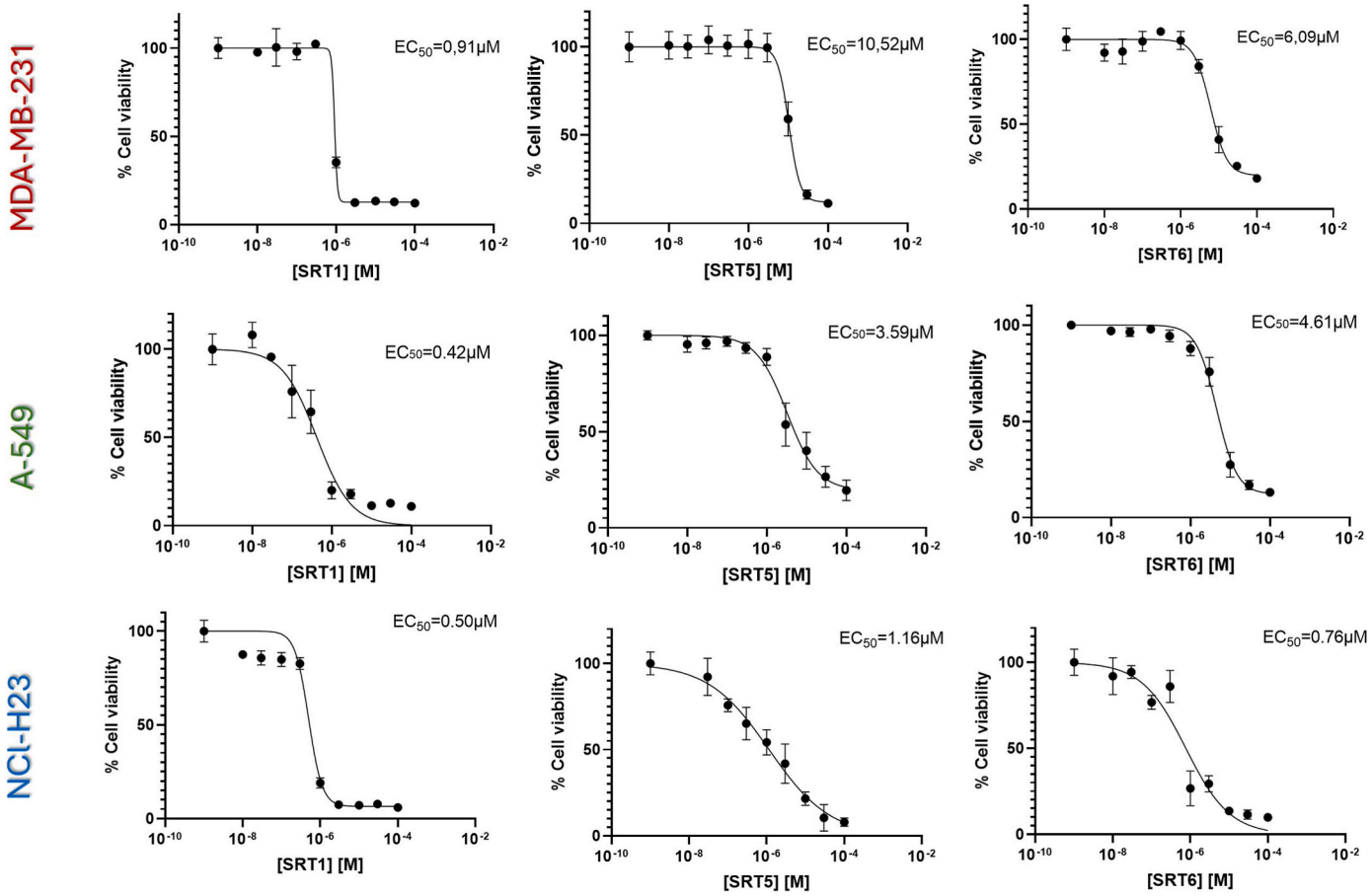

Fig. 4. Dose-response curves for the most active compounds **SRT1, SRT5** and **SRT6** against MDA-MB-231, A549 and NCI–H23 cells after 5 days of treatment. Error bars: ±SD from n = 3.

μM, respectively). Similarly, substitution with a CF_3 group at R_4 significantly reduced activity (**SRT9**, EC_{50} = 48.89 μM), except for **SRT10** (EC_{50} = 10.44 μM). Furthermore, the presence of a NO_2 group at the *para* position of the sulfonate ester improved the activity in all cases compared to the CH_3 group, as evidenced by the lower EC_{50} values (**SRT6**<**SRT5**, **SRT8**<**SRT7** and **SRT10**<**SRT9**). This suggests that the NO_2 group may enhance the stability of the compound's interaction with the biological target.

2.4. Evaluation of the role of CD44 inhibition by molecular dynamics, competitive binding assays and cell viability in MDA-MB-231 cells

We first performed a Molecular Dynamics (MD) study to gain deeper insight into the interactions of the compounds with CD44 and to further elucidate the stability and behaviour of their complexes over time. Five independent MD simulations were conducted for the most active compounds, **SRT5** and **SRT6**. The selected starting poses, characterized by the lowest binding energies and key interactions with critical residues, were used as initial configurations. Each simulation was run for 200 ns to ensure sufficient sampling of the conformational space and to capture the dynamic behaviour of the ligand–protein complexes.

The binding duration of the varied significantly across the replicas for both compounds. For **SRT6**, binding times ranged from 12 ns to 192 ns, while for **SRT5** they ranged from 12 ns to 112 ns. This wide range suggests potential instability or the existence of multiple binding modes. The variability indicates that the ligands may form transient rather than consistently stable interactions with the protein (Fig. 5).

Hydrogen bond (H-bond) analysis across all replicas revealed distinct interaction patterns with different residues. **SRT6** formed between five and eight H-bonds depending on the replica. Notably, Cys32 and Cys81 emerged as key residues, with Cys32 displaying the highest H-bond occupancy (9.01 %). In contrast, **SRT5** established only one to two H-bonds, primarily with Cys32 and Thr31, with Cys32 again showing the highest occupancy (>8 %).

Arg155 and Tyr34 are frequently involved in hydrogen bonding with both compounds, and Asn29 also interacts with **SRT6**, although all with relatively low occupancy. Additionally, residues - Tyr34, Gly44, Gln58, Glu79, Thr80, Arg82, Asn98, and Gln170 - appear in one or two replicates, also with low occupancies.

These data suggest that the compounds do not adopt a single dominant binding mode but instead explore multiple conformations, as illustrated in Fig. 5. Nevertheless, despite the low hydrogen bond occupancy in some replicas, the ligands remain bound for over 100 ns. This indicates that their stability may be significantly supported by additional interactions, such as π-π staking between guanidinium group of Arg155 and the THIQ ring or the other aromatic moieties, as well as hydrophobic and van der Waals contacts.

The results obtained in this study are consistent with previous findings for compound **SRT1**. [17] A key distinction between **SRT5**/**SRT6** and **SRT1** lies in their binding profiles: whereas **SRT1** primarily interacts with Arg155, the extended scaffolds **SRT5** and **SRT6** allow them to penetrate deeper into the binding site, establishing preferential contacts with residues such as Cys81, Cys32 and Thr31.

Taken together, these findings suggest that compounds **SRT5** and **SRT6** may act as competitors of HA for the binding groove. Computational analysis predicts that they interact with the same key residues within the CD44-HABD domain as those involved in HA recognition.

To determine the binding affinity of **SRT5** and **SRT6** to CD44, we

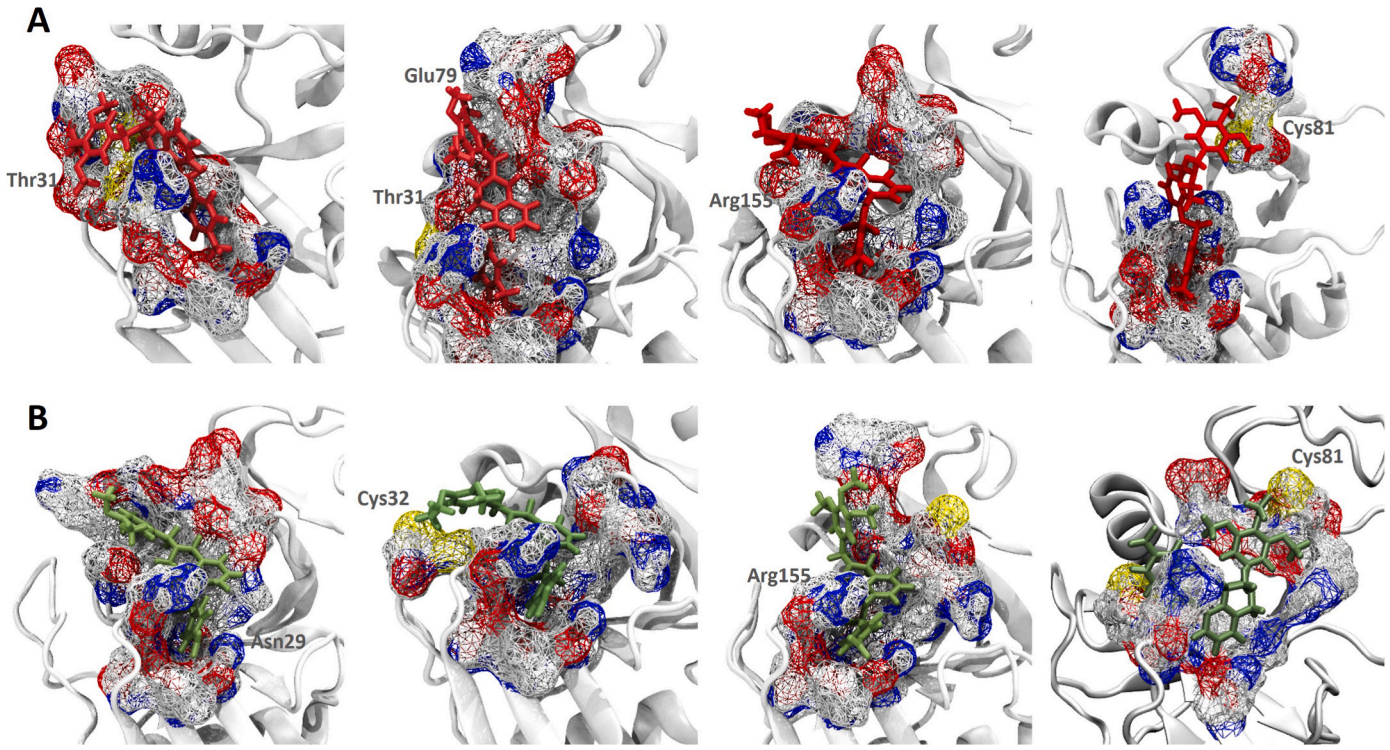

Fig. 5. Representative binding poses of **SRT5 (A)** and **SRT6 (B)** within the CD44-HABD observed during molecular dynamics simulations. CD44 is shown as a white NewCartoon representation (based on PDB ID: 5BZK). **SRT5** and **SRT6** are depicted in red and green licorice, respectively. Key residues forming hydrogen bonds within 3 Å of the ligands are highlighted in wireframe. (For interpretation of the references to colour in this figure legend, the reader is referred to the Web version of this article.)

performed a competitive binding assay using a fluorescently labeled hyaluronic acid derivative (HA-FITC) as a natural ligand for CD44. MDA-MB-231 cells were pre-incubated with **SRT5** and **SRT6** for 30 min at 4 °C and physiological pH to facilitate binding to CD44 receptors on the cell surface. The cells were then incubated with HA-FITC for 15 min at 4 °C and fluorescence was measured by flow cytometry. The IM7 anti-CD44 antibody was used as a positive control and cells treated with unlabelled HA served as a negative control.

Pre-incubation with **SRT5** and **SRT6** showed a significant reduction in fluorescence intensity (1.1-fold and 1.6-fold respectively, Fig. 6) compared to cells incubated with HA-FITC and those pre-treated with the anti-CD44 monoclonal antibody. These results strongly suggest that both compounds effectively compete with HA-FITC for CD44 binding sites, demonstrating their ability to inhibit the HA-CD44 interaction. The results for **SRT5** and **SRT6** are consistent with our earlier findings for **SRT1**. [17]

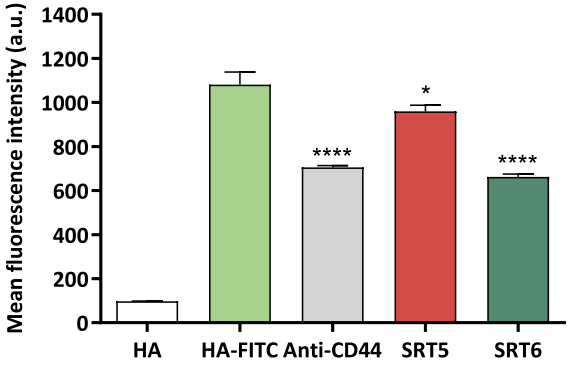

Fig. 6. HA-CD44 competitive assay. Flow cytometry analysis of MDA-MB-231 cells after treatment with **SRT5** and **SRT6** (30 min, 4 °C) followed by incubation with HA-FITC (15 min, 4 °C). Cells incubated with HA-FITC and non fluorescently labeled HA were used as positive and negative controls, respectively. Error bars: ±SD from n = 3; ***$p < 0.001$, ****$p < 0.0001$ vs. control group (ANOVA).

To elucidate the contribution of CD44 inhibition to the observed effect on cell viability in MDA-MB-231 cancer cells, a competitive binding experiment was conducted (Fig. 7). Cells were preincubated with the anti-CD44 antibody IM7 prior to exposure to the target compounds (**SRT5** and **SRT6**), resulting in a significant reduction in antiproliferative activity compared to untreated controls (14 % and 13 %, respectively). The effects observed with **SRT5** and **SRT6** were slightly lower than those previously reported for **SRT1** [17] suggesting that preincubation with the antibody effectively blocks CD44 binding sites, thereby preventing the ligands from recognizing their epitopes. These results support the conclusion that the therapeutic effects of both compounds are closely linked to their ability to interact with CD44. The experimental results confirm that, as suggested by the MD simulations, **SRT5** and **SRT6** are capable of binding to the CD44 receptor and inhibiting its interaction with hyaluronic acid (HA), similarly to the previously reported compound **SRT1**.

2.5. Antiproliferative activity in A549 and NCI–H23 lung cancer cells

CD44 plays a critical role in the progression of lung cancer by promoting cell proliferation, invasion, and metastasis [19]. To further explore the anticancer potential of compounds **SRT1-SRT10**, their antiproliferative activity was also evaluated against two $CD44^+$ human lung cancer cell lines, A549 and NCI–H23 (Table 1, Fig. 4 and Figs. S2–S4). CD44 overexpression in these cell lines was confirmed by flow cytometry using the anti-CD44 antibody IM7 (Fig. S1). Compound **SRT1** was included in this study as its antitumor activity had previously only been investigated in MDA-MB-231 breast cancer.

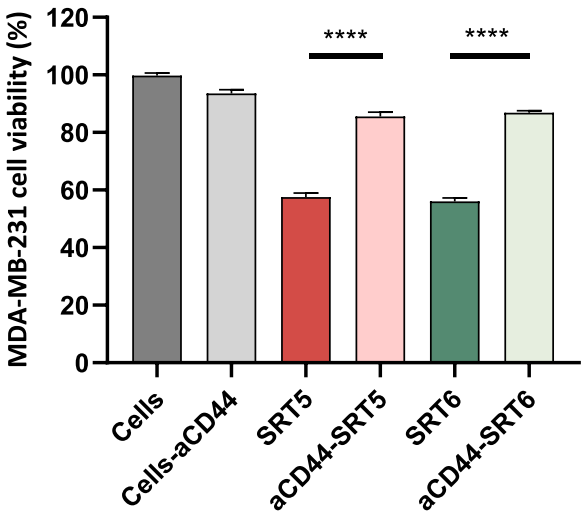

Fig. 7. MDA−MB−231 cell viability after treatment with **SRT5** and **SRT6** (EC_{50}). aCD44-**SRT5** and aCD44-**SRT6**: cells preincubated with antiCD44 antibody IM7 (30 min). **SRT5** and **SRT6**: cells without preincubation with IM7. Untreated cells (Cells) and cells treated with IM7 (Cells-aCD44) were used as controls. Error bars: ±SD from n = 3; ****$p < 0.0001$ (Student's *t*-test).

The structure-activity relationships in A549 cells are similar to those observed in MDA-MB-231: i) incorporation of the sulfonate ester moiety generally reduces the antiproliferative effect, with the exception of **SRT10**; ii) a consistent trend in activity was observed for the substituents at positions $R_{3'}$, $R_{4'}$ and $R_{5'}$ (3,4,5-OCH_3> 3,5-OCH_3> 4-CF_3> 4-NO_2) and iii) the presence of a NO_2 group at the *para* position of the sulfonate ester typically enhanced activity compared to a CH_3 group.

In NCI–H23 cells, the introduction of the sulfonate ester does not adversely affect activity, in fact, all compounds from **SRT5** to **SRT10** exhibited EC_{50} values below 5 μM. Notably, **SRT7**, **SRT8** and **SRT9**, **SRT10** showed significantly higher activity than their corresponding **SRT2** and **SRT3** derivatives. Furthermore, unlike the results observed in MDA-MB-231 and A549 cells, no significant differences in activity were found in this cell line with respect to either the substitution pattern on the aromatic ring ($R_{3'}$, $R_{4'}$ and $R_{5'}$) or the nature of the *para* substituent on the sulfonate ester.

Overall, the target compounds **SRT1-SRT10** exhibited greater activity against NCI–H23 cells than A549 cells. Notably, **SRT1** demonstrated strong inhibitory activity in both cell lines (EC_{50} A549 = 0.88 μM and EC_{50} NCI–H23 = 0.42 μM, Fig. 4), underscoring its potential as a lead compound. Among the modified esters, **SRT5** and **SRT6**, also showed enhanced antiproliferative effects in both lung cancer models, further emphasizing their promise in anticancer therapy (EC_{50} A549 = 4.05 μM and EC_{50} NCl–H23 = 5.00 μM for **SRT5** and EC_{50} A549 = 3.11 μM and EC_{50} NCI–H23 = 4.17 μM for **SRT5**, Fig. 4).

For further investigation, we selected **SRT1**, **SRT5** and **SRT6** to explore the mechanisms underlying their cell death-inducing effects. These studies primarily focused on apoptosis assays in lung cancer cells, as apoptosis plays a critical role in programmed cell death. Understanding how these compounds influence apoptosis will provide valuable insights into their anticancer potential.

2.6. Apoptosis studies using annexin V binding assay in NCl–H23 cancer cells

Apoptosis is a tightly regulated form of programmed cell death that plays a critical role in maintaining tissue homeostasis and eliminating damaged or potentially harmful cells. It is characterized by a series of morphological and biochemical events, including chromatin condensation, DNA fragmentation, membrane blebbing, and ultimately, the formation of apoptotic bodies [20]. Induction of apoptosis is a desirable outcome in cancer therapy, as it enables the selective elimination of tumor cells without triggering the inflammatory responses typically associated with necrosis [21],[22].

Annexin V is a phospholipid-binding protein with high affinity for phosphatidylserine (PS), a lipid that is typically confined to the inner leaflet of the plasma membrane but is externalized during the early stages of apoptosis [23]. The detection of PS exposure through Annexin V-FITC binding serves as a sensitive and early marker of apoptotic cell death.

NCI–H23 cells were treated with **SRT1**, **SRT5** and **SRT6** and analyzed by flow cytometry using Annexin V (Fig. 8). In untreated cells (negative control), only 5.24 % were Annexin V positive, whereas the positive control (H_2O_2) induced a significant apoptotic response, with 84.81 % Annexin V positivity.

Among the compounds tested, **SRT1** caused a significant increase in Annexin V staining (47.38 %, $p < 0.0001$), indicating a strong pro-apoptotic effect. **SRT5** induced a mild but statistically significant increase (21.37 %, $p < 0.05$), while **SRT6** showed no significant difference compared to the negative control (14.54 %, ns).

To further differentiate between early apoptosis, late apoptosis, and necrosis, we employed a combination of Annexin V staining and propidium iodide (PI), a membrane-impermeable DNA intercalating dye. Annexin V positive and PI negative cells are indicative of early apoptosis, while cells that are positive for both Annexin V and PI represent late apoptotic or secondary necrotic stages, where membrane integrity is compromised. In contrast, PI positive/Annexin V negative cells are typically associated with primary necrosis, and double negative cells are considered viable [24].

This dual staining approach enabled us to not only assess of the cell death but also track the progression of the process, offering valuable insights into the compounds' mechanism of action and their potential therapeutic relevance.

In untreated NCI–H23 control cells, only 3.3 % of cells were in early apoptosis, 3.6 % in late-stage apoptosis, and 2.5 % undergoing necrosis. Upon treatment with **SRT1**, a substantial shift was observed: the early apoptotic population increased to 26.06 %, and late apoptosis rose to

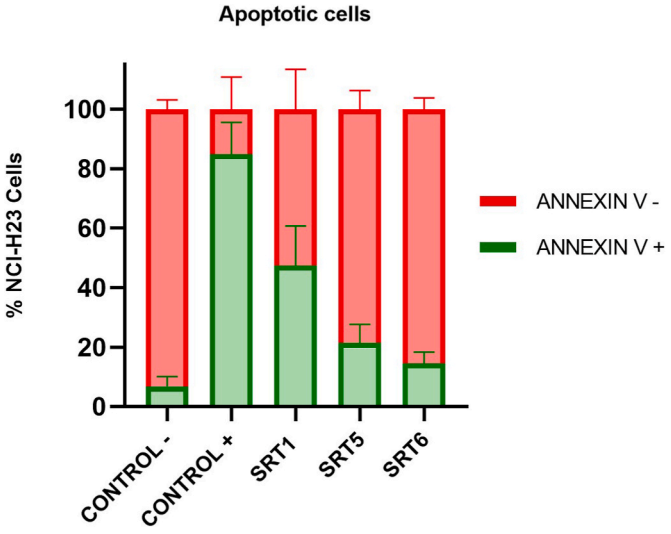

Fig. 8. Percentage of apoptotic (Annexin V positive, green) *versus* non-apoptotic (Annexin V negative, red) NCI–H23 cells after treatment with the positive control and compounds **SRT1**, **SRT5** and **SRT6**. Bars represent mean ± SD from at least three independent experiments. (For interpretation of the references to colour in this figure legend, the reader is referred to the Web version of this article.)

21.31 % (Fig. 9). These changes correspond to a 47 % increase in the overall proportion of apoptotic cells, indicating that **SRT1** significantly compromises cell viability by promoting programmed cell death. This pronounced pro-apoptotic effect highlights the potential of **SRT1** as a potent inducer of apoptosis in lung cancer cells. In contrast, **SRT5** and **SRT6** did not induce a marked apoptotic response. Both compounds showed no significant difference from the negative control, with **SRT5** resulting in 9.58 % early and 11.79 % late apoptosis, and **SRT6** showing 7.36 % early and 7.18 % late apoptosis. These findings suggest that apoptosis is not the primary mechanism by which **SRT5** and **SRT6** exert their antiproliferative effects, indicating that alternative, non-apoptotic pathways may be involved in mediating their cytotoxicity.

The pronounced difference in apoptosis induction between **SRT1** and its ester derivatives underscores the distinct mechanism of action of **SRT1**. Unlike **SRT5** and **SRT6**, which exhibit antiproliferative effects likely through alternative, non-apoptotic pathways, **SRT1** induces a robust apoptotic response, leading to significant cancer cell death. This mechanistic divergence is critical for understanding the therapeutic potential of these compounds, as it may influence their application across different cancer types or in combination therapies.

2.7. Evaluation of the selectivity index in lung cells

The SI is a crucial parameter for evaluating the therapeutic potential of anticancer compounds. It is defined as the ratio of the compound's cytotoxic activity against cancer cells to its cytotoxic activity against normal, healthy cells. A higher SI indicates greater selectivity for cancer cells, indicating a more favorable therapeutic window and reduced likelihood of adverse effects on normal tissues. In this study, we determined the SI values for compounds **SRT1**, **SRT5**, and **SRT6** by comparing their antiproliferative activity in two lung cancer cells lines, A549 and NCI–H23, with their effects on the non-tumorigenic human lung fibroblast cell line CCD-16Lu (Table 2). This analysis provides valuable insights into the safety and efficacy profiles of these compounds and supports their potential for future clinical development.

SRT1 demonstrated the highest SI with values of 37.9 in A549 and 79.47 in NCI–H23 cells, indicating a strong preferential activity toward cancer cells over normal cells. This high level of selectivity suggests that **SRT1** possesses a favorable therapeutic window, supporting its potential as a promising candidate for further development.

SRT5 and **SRT6** also exhibited notable SI values. Specifically, **SRT5** showed SI values of 10.31 for A549 and 13.42 for NCI–H23, while **SRT6** recorded SI values of 10.01 for A549 and 36.54 for NCI–H23. These findings confirm that both compounds maintain a degree of selectivity for cancer cells, though to a lesser extent than **SRT1**.

The consistency higher selectivity indices in NCI–H23 cells compared to A549 suggest that these compounds may exert particularly potent effect against this lung cancer subtype.

2.8. Kinase inhibition study

To further investigate the mechanism of action of **SRT1**, **SRT5**, and **SRT6**, we examined their inhibition profiles against a panel of kinases involved in cellular signaling pathways that regulate cell growth, proliferation, differentiation, and survival. These kinases are often dysregulated in cancer and represent critical targets in the development of anticancer therapies.

The 33 selected kinases were chosen for their known involvement in the CD44 signaling pathway. Activation of CD44 triggers downstream signaling cascades, such as the PI3K/AKT and MAPK/ERK pathways, which are essential for tumor growth and metastasis [25],[26]. For instance, EGFR and HER2 are receptor tyrosine kinases that, upon

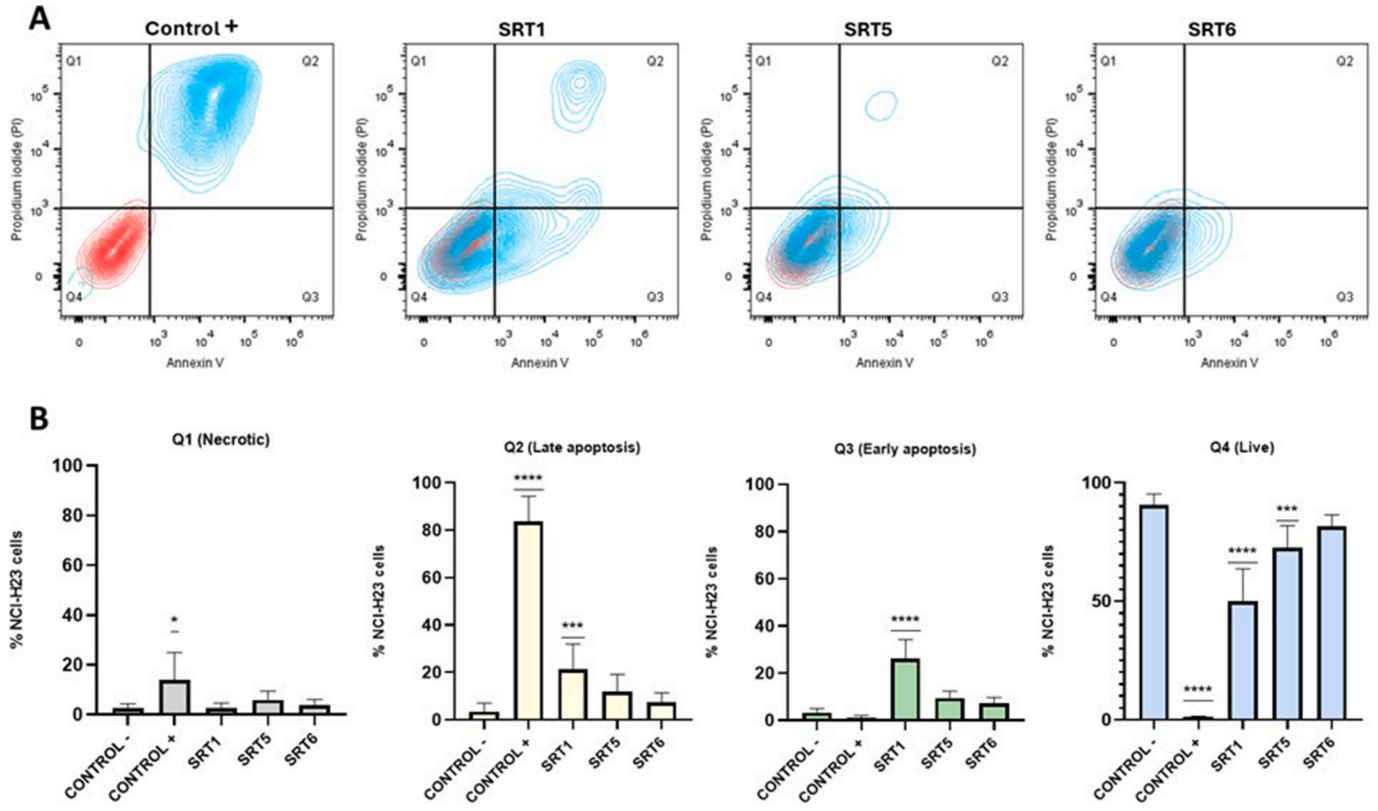

Fig. 9. A) Apoptosis images of NCI–H23 lung cancer. Red: negative control. Blue: treated cells. **B)** Percentage of NCI–H23 cells according to the detected cell death mechanism. Data are presented as mean ± SD from three independent experiments. Statistical analysis was performed using two-way ANOVA followed by Dunnett's multiple comparisons test, comparing each treatment to the untreated control. Significance levels: $*p < 0.05$, $**p < 0.01$, $****p < 0.0001$. (For interpretation of the references to colour in this figure legend, the reader is referred to the Web version of this article.)

Table 2
EC_{50} values (μM) obtained after treatment of A549, NCI–H23 and CCD-16Lu cell lines with **SRT1**, **SRT5** and **SRT6** and the SI over A549 and NCI–H23 cells.

Compounds	EC_{50} A549	EC_{50} NCI–H23	EC_{50} CCD-16Lu	SI (CCD-16Lu/A549)	SI (CCD-16Lu/NCI–H23)
SRT1	0.88 ± 0.31	0.42 ± 0.07	33.38 ± 4.10	37.93	79.47
SRT5	4.05 ± 1.36	3.11 ± 1.83	41.76 ± 5.82	10.31	13.42
SRT6	5.00 ± 0.83	1.37 ± 0.52	50.06 ± 8.66	10.01	36.54

All experiments were conducted in triplicate and gave similar results. Data are mean ± SEM of three independent experiments.

activation, initiate the RAS-RAF-MEK-ERK signaling cascade, promoting increased cell proliferation and survival [27]. Similarly, the PI3K/AKT pathway-through kinases such as AKT1 and AKT2 - regulates key cellular processes including metabolism, growth, and survival. [27] SRC kinase is another critical component of this network, influencing various cellular behaviors such as proliferation, survival, and migration [28]. Table 3 presents the results for residual kinase activity at two concentrations, 5 μM and 50 μM.

The kinase inhibition study revealed distinct differences in the inhibition profiles of compound **SRT1** and its ester derivatives, **SRT5** and **SRT6**. At a concentration of 5 μM, all three compounds exhibited less than 25 % inhibition across the panel of the selected kinases. However, at 50 μM, **SRT5** and **SRT6** demonstrated significantly increased inhibitory activity, indicating a dose-dependent effect and suggesting potential engagement with kinases involved in CD44-mediated signalling pathways.

For example, **SRT1** showed minimal inhibition of SRC kinase, with residual activities of 88 %, whereas **SRT5** and **SRT6** exhibited substantial inhibition, with residual activities of 16 % and 14 % respectively. This marked inhibition suggests that **SRT5** and **SRT6** may exert their antiproliferative effects, at least in part, through the inhibition of SRC kinase - a key component of the CD44 signaling pathway. Given that the SRC kinase regulates essential cellular processes such as proliferation, survival, and migration; its inhibition could significantly disrupt these pathways in $CD44^+$ breast cancer cells.

Additionally, **SRT6** demonstrated strong inhibition of EGFR and ERBB2, with residual activities of 24 % and 21 % respectively. These findings suggest that **SRT6** may act on multiple kinases involved in the CD44 signaling cascade, thereby contributing to its potent antiproliferative activity. This multi-targeted inhibition profile reinforces the potential of **SRT6** as a promising therapeutic agent for $CD44^+$ cancers.

The inhibition of these kinases by compounds **SRT5** and **SRT6** suggests that their antiproliferative effects may be mediated through disruption of the signaling pathways, thereby impairing the malignant behavior of $CD44^+$ cancer cells. In contrast, the limited kinase inhibition observed for **SRT1** indicates that its mechanism of action may involve alternative pathways or molecular targets not examined in this study.

2.9. In silico prediction of physicochemical parameters and ADME properties

2.9.1. Physicochemical parameters

A critical aspect of drug development is the optimization of the route of administration, with oral delivery often being the preferred option. A commonly used method to predict oral bioavailability involves evaluating compliance with Lipinski's Rule of Five and Veber's rules. In this study, these criteria were assessed for the compounds with the most promising biological activity (**SRT1**, **SRT5**, and **SRT6**) using the freely available online tool at: http://biosig.unimelb.edu.au/pkcsm/prediction. The results are presented in Table 5. The SMILES representations of the compounds were retrieved from PubChem (https://pubchem.ncbi.nlm.nih.gov).

According to Table 4, the compound **SRT1** complies fully with both the Lipinski's and Veber's rules suggesting favorable oral biovailability. The derivative **SRT5** does not violate any of Lipinski's criteria; however, it presents a topological polar surface area (TPSA) slightly above 140 $Å^2$, which may affect permeability. Compound **SRT6** satisfies three out of four Lipinsky parameters with molecular weight slightly exceeding 500 Da. Despite these minor deviations, the results indicate that all three compounds are likely to exhibit good oral bioavailability.

2.9.2. ADME properties

Pharmacokinetic properties - absorption, distribution, metabolism, and excretion (ADME) - are critical considerations in the early stages of drug development, as they can significantly reduce both time and costs. To evaluate these properties in the most active compounds, we employed the freely accessible online tool available at: http://biosig.unimelb.edu.au/pkcsm/prediction. The predicted ADME parameters are summarised in Table 5.

High absorption is considered 70–100 %, medium absorption 20–70 %, and low absorption 0–20 %. [29] These compounds exhibit high intestinal absorption, supporting the hypothesis that they could be promising candidates for the development of oral drugs.

Blood–brain barrier (BBB) penetration is considered high for compounds with a log BB > 0.3, moderate for log BB values between 0 and 0.3, and low for log BB < 0. In the case of these compounds, all log BB values are below zero, indicating minimal or no ability to cross the BBB. This property is desirable for standard chemotherapy treatments targeting peripheral cancers (*e.g.* breast, lung or colon), where BBB penetration is unnecessary and may lead to unwanted side effects in the central nervous system.

In silico predictions further indicate that **SRT1** is not an inhibitor of the cytochrome P450 enzymes CYP3A4 and CYP2C19, suggesting that it is likely to be metabolized effectively without accumulating in plasma and causing toxicity. **SRT5** and **SRT6** were predicted to inhibit only cytochrome CYP2C19, implying a potentially lower risk of metabolic interactions compared to broader-spectrum inhibitors.

Total clearance values, expressed as log ml/min/kg are used to estimate drug elimination rates: values > 0 indicate rapid clearance, values between 0 and -1 suggest moderate clearance, and values < -1 denote slow elimination. All compounds in this study exhibited high clearance values (>0), which reduces the risk of drug accumulation and associated adverse effects.

The drug-likeness score (Table 5) provides a theoretical estimate of a compound's similarity to a known drugs and its potential as a therapeutic agent. These scores were calculated using the freely available MolSoft online platform (https://www.molsoft.com/servers.html). A value close to 1 indicates ahigh likelihood of drug like properties [30]. The **SRT1**, **SRT5** and **SRT6** derivatives all exhibit predicted scores close to 1, supporting their potential as promising candidates for further drug development.

Overall, the *in silico* results provide a strong rationale for advancing these compounds to *in vivo* studies.

3. Conclusion

This study successfully builds upon previous work with the lead compound **SRT1**, demonstrated potent anti-proliferative activity in breast cancer cells. By synthesizing and evaluating a series of derivatives (**SRT2-SRT10**), we assessed their efficacy in $CD44^+$ lung cancer models for the first time. The design of these new compounds was inspired by the structural features of **SRT1** with the aim of enhancing its biological activity and selectivity. Structure-activity relationship studies in $CD44^+$

Table 3
Selective profiles of **SRT1**, **SRT7** and **SRT8** against 31 protein kinases and 2 lipid kinases.

Compound	SRT1	SRT1	SRT5	SRT5	SRT6	SRT6
Assay concentration	5 μM	50 μM	5 μM	50 μM	5 μM	50 μM
AKT1	92	87	101	100	96	81
AKT2	100	92	93	111	94	64
AKT3	118	115	116	103	116	98
EGFR	120	102	106	74	91	24
ERBB2	103	97	88	31	86	21
ERBB4	110	89	104	54	65	21
ERK1	106	104	104	76	109	50
ERK2	101	98	94	77	93	48
ERK5	92	97	103	83	90	51
ERK7	107	95	101	109	111	57
MAP3K1	99	94	105	104	91	61
MAP3K10	111	106	100	56	109	24
MAP3K11	105	89	116	117	103	69
MAP3K7/MAP3K7IP1	98	96	98	173	97	129
MAP3K9	108	101	104	99	107	62
MAP4K1	122	119	129	144	124	134
MAP4K2	104	94	88	87	92	72
MAP4K4	98	93	104	90	93	75
MAP4K5	103	103	112	111	102	90
MAPKAPK2	95	76	60	27	65	17
MAPKAPK3	104	98	103	92	95	61
MAPKAPK5	129	134	104	60	100	40
MEK1	128	120	108	116	112	105
MEK2	106	92	103	118	109	75
MEK5	88	95	103	105	99	56
MEKK2	102	106	112	110	108	76
MEKK3	124	137	128	125	132	85
RAF1 YDYD	105	94	113	70	104	61
SRC	102	88	97	16	62	14
TGFBR1	96	88	104	84	96	59
TGFBR2	107	101	116	73	101	41
PIK3C3	98	101	102	109	128	108
PIK3CG	102	106	104	151	101	91

Residual activity ≤ 25
Residual activity > 25 % and ≤ 50 %
Residual activity > 50 % and ≤ 75 %
Residual activity > 75 %

Table 4
Calculated Lipinski and Veber parameters for compounds **SRT1**, **SRT5** and **SRT6**.

Compounds	MW	LogP	HBD	HBA	nVs	nRB	TPSA
Lipinski[a]	≤500	≤5	≤5	≤10	–	–	–
Veber[b]	–	–	–	–	–	≤10	≤140
SRT1	329.40	2.97	1	5	0	5	141.93
SRT5	483.58	4.34	0	7	0	8	200.50
SRT6	514.55	3.94	0	9	1	9	208.79

[a] Lipinski reference values
[b] Veber reference values; MW, Molecular weight; LogP, lipophilicity (O/W); HBD, Number of hydrogen bond donors; HBA, Number of hydrogen bond acceptors; nVs, Number of Lipinski rule violations; nRB, Number of rotatable bonds; TPSA, molecular polar surface area (TPSA) ($Å^2$).

Table 5
ADME properties of compounds **SRT1**, **SRT5** and **SRT6.**

Compounds	HIA (%)	BBB (logBB)	CYP2C9 inhibition	CYP3A4 inhibition	Total clearance (log ml/min/kg)	Drug-likeness score
SRT1	89.85	−0.26	Non	Non	1.04	1.07
SRT5	91.99	−0.545	Non	Yes	0.56	0.82
SRT6	100	−1	Non	Yes	0.30	0.51

HIA, Human Intestinal Absorption (%); BBB, Blood-Brain Barrier penetration (log BB); Cytochrome CYP2C9; Cytochrome CYP3A4; Total clearance (log ml/min/kg).

breast cancer cells identified the sulfonates esters of **SRT1**, **SRT5** and **SRT6**, as the most promising derivatives.

Cell viability, competitive binding assays and molecular dynamics studies demonstrated effective inhibition of HA-CD44 binding by compounds **SRT5** and **SRT6**, similar to **SRT1**. These findings confirm that **SRT5** and **SRT6** are potent CD44 inhibitors, capable of disrupting the HA-CD44 interaction that is critical for cancer cell proliferation and survival.

In lung cancer models, **SRT1** exhibited the most potent antiproliferative effects against $CD44^+$ lung cancer cell lines A549 and NCI–H23, with EC_{50} values of 0.88 μM and 0.42 μM, respectively. **SRT5** and **SRT6** also displayed significant activity, particularly against NCI–H23 cells, reinforcing their potential as anticancer agents. Notably, **SRT1** induced significant apoptosis in NCI–H23 cells, whereas **SRT5** and **SRT6** did not induce apoptosis, suggesting that their antiproliferative effects may be mediated by alternative mechanisms. The SI values for **SRT1**, **SRT5** and **SRT6** indicated a strong selectivity for cancer cells over normal cells. **SRT1** was nearly 80 times more active in NCl–H23 cells than in healthy lung cells, highlighting its promise for targeted cancer therapy.

Kinase inhibition assays revealed that **SRT5** and **SRT6** significantly inhibit key kinases involved in the CD44 mediated signaling. In particular, both compounds substantially inhibited SRC kinase, a critical component of the CD44 pathway. In contrast, **SRT1** showed minimal kinase inhibition, suggesting a distinct mechanism of action.

In silico ADME predictions further support the potential of **SRT1**, **SRT5** and **SRT6** as orally administered anticancer agents, indicating preliminary favorable pharmacokinetic properties that require experimental validation.

Taken together, these findings highlight the potential of these *N*-benzyl THIQ derivatives, as selective and effective therapeutic agents for lung cancer. Further studies are warranted to investigate their distinct mechanisms of action, optimize their efficacy and safety profiles, and explore their full therapeutic potential. In particular, *in vivo* evaluation is planned to assess its pharmacokinetic profiles, efficacy, and safety in a more physiologically relevant context.

4. Experimental section

4.1. Chemistry

4.1.1. General methods

Analytical thin layer chromatography was performed using Merck Kieselgel 60 F_{254} aluminium plates and visualized by UV light (254 nm). Evaporation was carried out *in vacuo* in a Büchi rotary evaporator, and the pressure controlled by a Vacuubrand CVCII apparatus. Purifications were carried out through preparative layer chromatography or by flash column chromatography using silica gel 60 with a particle size of 0.040–0.063 nm (230–440 mesh ASTM). Melting points were taken in open capillaries on a Stuart Scientific SMP3 electrothermal melting point apparatus and are uncorrected.

^{1}H NMR and ^{13}C NMR spectra were obtained using Bruker Avance NEO spectrometers with Smart Probe BBFO equipped, operating at 400.57 MHz for ^{1}H and 100.73 MHz for ^{13}C, at 499.79 MHz for ^{1}H and 125.68 MHz for ^{13}C, or 600.25 MHz for ^{1}H and 150.95 MHz for ^{13}C, in the deuterated solvents. The multiplicity of each signal is given as s (singlet), d (doublet), dd (double doublet), t (triplet), q (quadruplet) and m (multiplet). *J* values are expressed in Hz. The compounds were dissolved in deuterated solvents ($CDCl_3$, MeOD and DMSO). High-resolution electrospray ionization time-of-flight (ESI-TOF) mass spectra were carried out on a Waters LCT Premier Mass Spectrometer. The samples studied were dried in a Gallencamp oven at reduced pressure with P_2O_5 inside.

All chemical reagents were supplied by Sigma-Aldrich, Thermo Fisher Scientific, VWR International Ltd and Fluorochem. The intermediate 1,2,3,4-tetrahydroquinolin-5-ol acetate and compound **SRT1** were synthesized as previously described [17]. HPLC profile of compound **SRT1** is included in the Supporting Information (Fig. S5).

4.1.2. General procedure for the synthesis of compounds SRT2 - SRT4

A solution of 1,2,3,4-tetrahydroquinolin-5-ol acetate (1 eq.) and Et_3N (1eq.) in absolute EtOH (3 ml/mmol) was stirred at rt for 1 h. Then, another equivalent of Et_3N and the corresponding benzyl chloride or benzyl bromide derivative (1 eq.) were added at 0 °C. The reaction mixtures were stirred at 0 °C for 10 min and at room temperature rt overnight. The EtOH was removed under vacuum and the residue was extracted with Cl_2CH_2 and washed with H_2O and brine. The organic phases were dried over anhydrous Na_2SO_4, filtered and concentrated under vacuum. The residue was purified by flash chromatography using EtOAc/hexane in different ratios as solvent.

*4.1.2.1. 2-(3,5-Dimethoxybenzyl)-1,2,3,4-tetrahydroisoquinolin-5-ol (**SRT2**).* Purification in EtOAc/hexane 1:3. White solid; 44 % yield. **Mp:** 180-183°C. **^{1}H NMR** (400 MHz, MeOD) δ (ppm): 6.94 (t, $J = 7.8$ Hz, 1H), 6.61–6.59 (m, 3H), 6.51 (d, $J = 7.6$ Hz, 1H), 6.42 (t, $J = 2.3$ Hz, 1H), 3.78 (s, 6H), 3.67 (s, 2H, 3.63 (s, 2H), 2.82–2.79 (m, 4H). **^{13}C NMR** (126 MHz, MeOD) δ (ppm): 161.92, 155.64, 139.87, 135.70, 127.25, 121.69, 118.03, 112.96, 108.09, 100.35, 63.27, 56.24, 55.24, 51.17, 23.54.

HRMS (*m/z*): calcd. for $C_{18}H_{22}NO_3$ $[M+H]^+$ 300.1600, found: 300.1574.

*4.1.2.2. 2-(4-(4-(Trifluoromethyl)benzyl)-1,2,3,4-tetrahydroisoquinolin-5-ol **(SRT3)**.* Purification in EtOAc/Hexane 1:4. White solid; 69 % yield. **Mp:** 185-186°C .**^{1}H NMR** (400 MHz, MeOD) δ (ppm): 7.67 (d, J = 8.2 Hz, 2H) 7.61 (d, J = 8.2 Hz), 6.95 (t, J = 7.8 Hz), 6.61 (dd, J = 7.9, 1.0 Hz), 6.51 (dd, J = 7.6, 1.0Hz, 1H), 3.78 (s, 2H), 3.60 (s, 2H), 2.78 (s, 4H).**^{13}C RMN** (151 MHz, MeOD) δ (ppm) 155.88, 143.34, 136.65, 130.99, 129.23 (q, J = 31.6 Hz), 127.42, 126.03, 124.36 (q, J = 271 Hz), 122.24, 118.68, 113.21, 62.69, 57.25, 51.80, 24.52. **HRMS** (*m/z*): calcd. for $C_{17}H_{17}F_3NO$ $[M+H]^+$ 308.1262, found 308.1293.

*4.1.2.3. 2-(4-Nitrobenzyl)-1,2,3,4-tetrahidroisoquinolin-5-ol **(SRT4)**.* Purification in EtOAc/Hexane 1:3. Yellow oil; 20 % yield. **^{1}H NMR** (400 MHz, MeOD) δ (ppm): 8.25 (d, J = 8.7 Hz, 2H), 7.70 (d, J = 8.6 Hz, 2H), 6.96 (t, J = 7.9 Hz, 1H), 6.63 (d, J = 7.9 Hz, 1H), 6.51 (d, J = 7.6 Hz, 1H), 4.12 (s, 2H), 3.89 (s, 2H), 3.10 (t, J = 6.2 Hz, 2H), 2.86 (t, J = 6.2 Hz, 2H). **^{13}C NMR** (126 MHz, MeOD) δ (ppm): 156.32, 149.55, 142.61, 133.67, 132.31, 128.30, 124.56, 120.96, 118.54, 113.96, 61.13, 55.98, 51.60, 23.19. **HRMS** (*m/z*): calcd. for $C_{16}H_{17}N_2O_3$ $[M+H]^+$ 285.1239, found 285.1232.

4.1.3. General procedure for the synthesis of compounds SRT5 - SRT10

To a solution of the corresponding alkylated derivative **SRT1** - **SRT4** (1 eq.) and TEA (1.2 eq.) in EtOH (3 mL/mmol), the corresponding 4-methylbenzenesulfonyl or 4-nitrobenzenesulphonyl chloride (1.1 eq.) was added for 10 min at 0 °C. The mixture was stirred at rt overnight. The EtOH was concentrated under vacuum and the residue was extracted with Cl_2CH_2. The organic phase was washed with H_2O and brine, dried over anhydrous Na_2SO_4, filtered and evaporated under vacuum. The residue was purified by flash chromatography using EtOAc/hexane in different ratios as solvent.

*4.1.3.1. 2-(3,4,5-Trimethoxybenzyl)-1,2,3,4-tetrahydroisoquinolin-5-yl-4-methylbenzenesulph**onate** **(SRT5)**.* Purification in EtOAc/Hexane 1:1. Yellow oil; 66 % yield. **^{1}H NMR** (400 MHz, $CDCl_3$) δ (ppm): 7.79 (d, J = 8.3 Hz, 2H), 7.34 (d, J = 8.3 Hz, 2H), 7.06 (t, J = 7.9 Hz, 1H), 6.93 (d, J = 7.6 Hz, 1H), 6.78 (d, J = 8.0 Hz, 1H), 6.60 (s, 2H), 3.85 (s, 6H), 3.84 (s, 3H), 3.61 - 3.57 (m, 4H), 2.77–2.74 (m, 2H), 2.65–2.62 (m, 2H) 2.45 (s, 3H). **^{13}C NMR** (101 MHz, $CDCl_3$) δ (ppm): 153.27, 148.01, 145.39, 137.26, 133.36, 129.96, 129.86, 128.35, 126.50, 125.41, 119.79, 105.91, 60.87, 56.21, 49.33, 29.70, 21.73. **HRMS** (*m/z*): calcd. for $C_{26}H_{30}NO_6S$ $[M+H]^+$ 484.1794, found 484.1807.

*4.1.3.2. 2-(3,4,5-Trimethoxybenzyl)-1,2,3,4-tetrahydroisoquinolin-5-yl-4-nitrobenzenesulfonate **(SRT6)**.* Purification in EtOAc/Hexane 1:4. Orange oil; 57 % yield. **^{1}H NMR** (400 MHz, $CDCl_3$) δ (ppm): 8.42–8.40 (m, 2H), 8.13–8.10 (m, 2H), 7.09 (t, J = 7.9 Hz, 1H), 6.97 (d, J = 7.6 Hz, 1H), 6.79 (d, J = 8.0 Hz, 1H), 6.62 (s, 2H), 3.85 (s, 9H), 3.66–3.62 (m, 4H), 2.78–2.70 (m, 4H). **^{13}C NMR** (101 MHz, $CDCl_3$) δ (ppm): 153.42, 151.20, 148.03, 142.08, 137.07, 137.30, 129.90, 129.81, 127.06, 126.30, 124.80, 119.62, 104.01, 65.70, 61.05, 60.51, 56.39, 49.36, 28.53. **HRMS** (*m/z*): calcd. for $C_{25}H_{27}N_2O_8S$ $[M+H]^+$ 515.1488, found 515.1470.

*4.1.3.3. 2-(3,5-Dimethoxybenzyl)-1,2,3,4-tetrahydroisoquinolin-5-yl-4-methylbenzenesulphonate **(SRT7)**.* Purification in EtOAc/Hexane 1:5. Yellow oil; 65 % yield. **^{1}H NMR** (400 MHz, $CDCl_3$) δ (ppm): 7.77 (d, J = 8.3 Hz, 2H), 7.33 (d, J = 8.0 Hz, 2H), 7.04 (t, J = 7.9 Hz, 1H), 6.90 (d, J = 7.5 Hz, 1H), 6.82 (d, J = 8.0 Hz, 1H), 6.53 (d, J = 2.3 Hz, 2H), 6.38 (t, J = 2.3 Hz, 1H), 3.81 (s, 6H), 3.60 (s, 2H) 3.57 (s, 2H), 2.70 (t, J = 5.6 Hz, 2H), 2.63 (t, J = 5.6 Hz, 2H), 2.46 (s, 3H). **^{13}C NMR** (101 MHz, $CDCl_3$) δ (ppm): 160.99, 148.30, 145.65, 140.86, 137.81, 133.61, 129.92, 128.77, 128.59, 126.41, 125.73, 119.63, 106.90, 99.53, 62.54, 55.80, 55.52, 49.6, 24.20, 21.87. **HRMS** (*m/z*): calcd. for $C_{25}H_{28}NO_5S$ $[M+H]^+$ 454.1688, found 454.1678.

*4.1.3.4. 2-(3,5-Dimethoxybenzyl)-1,2,3,4-tetrahydroisoquinolin-5-yl-4-nitrobenzenesulfonate **(SRT8)**.* Purification in EtOAc/Hexane 1:5. Yellow oil; 58 % yield. **^{1}H NMR** (400 MHz, $CDCl_3$) δ (ppm): 8.41–8.38 (m, 2H), 8.12–8.08 (m, 2H), 7.06 (t, J = 7.9 Hz, 1H), 6.95 (d, J = 7.4 Hz, 1H), 6.80 (d, J = 7.9 Hz, 1H), 6.53 (d, J = 2.2 Hz, 2H), 6.38 (t, J = 2.3 Hz, 1H), 3.78 (s, 6H), 3.63 (s, 2H), 3.61 (s, 2H), 2.73–2.68 (m, 4H). **^{13}C NMR** (101 MHz, $CDCl_3$) δ (ppm): 160.60, 150.76, 147.45, 141.51, 129.66, 129.39, 127.67, 126.47, 125.73, 124.15, 119.24, 106.68, 99.27, 61.71, 55.25, 54.66, 48.96, 29.40. **HRMS** (*m/z*): calcd. for $C_{24}H_{25}N_2O_7S$ $[M+H]^+$ 485.1382, found 485.1383.

*4.1.3.5. 2-(4-(Trifluoromethyl)benzyl)-1,2,3,4-tetrahydroisoquinolin-5-yl-4-methylbencenosulfonate **(SRT9)**.* Purification in EtOAc/Hexane 1:5. Colorless oil; 67 % yield. **^{1}H NMR** (400 MHz, $CDCl_3$) δ(ppm): 7.78 (d, J = 8.3 Hz, 2H), 7.59 (d, J = 8.1 Hz, 2H), 7.49 (d, J = 8.1 Hz, 2H), 7.34 (d, J = 8.3 Hz, 2H), 7.05 (t, J = 7.9 Hz, 1H), 6.90 (d, J = 7.5 Hz, 1H), 6.81 (d, J = 8.0 Hz, 1H), 3.71 (s, 2H), 3.62 (s, 2H), 2.74 (t, J = 5.7 Hz, 2H), 2.66 (t, J = 5.7 Hz, 2H), 2.46 (s, 3H).**^{13}C NMR** (101 MHz, $CDCl_3$) δ (ppm): 148.41, 145.60, 142.16, 137.13, 133.58, 130.13, 129.28, 129.0 (q, J = 32.6 Hz), 128.56, 126.57, 125.71, 125.12, 124.25 (q, J 272.0 Hz), 119.91, 61.73, 55.65, 49.90, 24.18, 21.97. **HRMS** (*m/z*): calcd. for $C_{24}H_{23}F_3NO_3S$ $[M+H]^+$ 462.1351, found 462.1380.

*4.1.3.6. 2-(4-(Trifluoromethyl)benzyl)-1,2,3,4-tetrahydroisoquinolin-5-yl-4-nitrobenzenesulfonate **(SRT-10)**.* Purification in EtOAc/Hexane 1:5. Yellow solid. **Mp**: 113°C – 114 °C. **^{1}H NMR** (400 MHz, $CDCl_3$) δ (ppm): 8.37–8.34 (m, 2H), 8.08–8.04 (m, 2H), 7.54 (d, J = 8.1 Hz, 2H), 7.43 (d, J = 8.0 Hz, 2H), 7.03 (t, J = 7.9 Hz, 1H), 6.90 (d, J = 7.5 Hz, 1H), 6.74 (d, J = 7.9 Hz, 1H), 3.66 (s, 2H), 3.57 (s, 2H), 2.69 (t, J = 5.5 Hz, 2H), 2.62 (t, J = 5.5 Hz, 2H). **^{13}C NMR** (101 MHz, $CDCl_3$) δ (ppm): 151.20, 147.87, 142.13, 141.89, 137.71, 129.74, 129.3 (q, J = 32.2 Hz), 128.83, 128.42, 126.66, 125.98, 125.42 (q, J = 272.0 Hz), 125.09, 124.44, 119.33, 61.80, 55.53, 49.61, 24.37. **HRMS** (*m/z*): calcd. for $C_{23}H_{20}F_3N_2O_5S$ $[M+H]^+$ 493.1045, found 493.1064.

4.2. Biology

4.2.1. General methods

A NuAire NU-4750E US AutoFlow incubator was used for cell culture. Cell-based experiments were carried out in a TELSTAR BIO II Class II A laminar flow cabinet. Flow cytometry assays were performed on a FACSCanto II system using the Flowjo® 10 software for analysis. Cell viability was carried out using a GloMax-Multi Detection System to measure fluorescence. Gibco (Thermo Fisher Scientific) was the supplier for the biological products including fetal bovine serum (FBS), trypsin-EDTA, DMEM, 1 % penicillin/streptomycin, and L-glutamine. Unlabelled HA (50 KDa) and HA-FITC (50 KDa) were purchased from HAworks LLC.

4.2.2. Cell culture

Human breast carcinoma (MDA-MB-231), lung cancer cell lines (A549, NCI–H23) and non-tumorigenic lung cell line (CCD16Lu) were provided by the Cell Bank the Center of Scientific Instrumentation of the University of Granada and obtained from the American Type Culture Collection. These cells were cultured in DMEM with serum (10 % FBS), L-glutamine (2 mM), and 1 % penicillin/streptomycin and incubated in a tissue culture incubator at 37 °C, 5 % CO_2 and 95 % relative humidity. Cells were frequently tested negative for mycoplasma infection.

4.2.3. Flow cytometry analysis of CD44 expression

Adherent MDA−MB−231, A-549 and NCl–H23 cells were trypsinized and counted in order to have 1 × 105 cells. Cells were centrifuged,

and after supernatant removal, cells were incubated with CD44 antibody (clone IM7, Thermo Fisher Scientific,USA) for 1h at RT. Cells were washed twice and incubated with a secondary antibody goat anti-rat AlexaFluor-647 (#A21247, Invitrogen) for 30min at rt (dark). After incubation, cells were centrifuged, pellets resuspended in PBS and samples analyzed by flow cytometry using FACSCanto II (Becton Dickinson & Co.) and Flowjo® 10 software.

4.2.4. Cell viability assays

Target compounds were dissolved in DMSO and stored at −20 °C. For each experiment, the stock solution (100 mM) was further diluted in culture media to obtain the desired concentrations. MDA-MB-231 (2000 cells/well), A549 and NCI–H23 (1500 cells/well) and CCD-16Lu (7500 cells/well) were seeded in a 96-well plate format and incubated for 24 h before treatment. Each well was then replaced with fresh media, containing target compounds (0.01–100 μM) and incubated for 5 days. Untreated cells (DMSO, 0.1 % *v/v*) were used as control to detect any undesirable effects of culture conditions on cell viability. Each experiment was performed in triplicates. PrestoBlue™ cell viability reagent (10 % *v/v*) was added to each well and the plate incubated for 120 min. Fluorescence emission was detected using a GloMax-Multi Detection System (excitation filter at 540 nm and emission filter at 590 nm). All conditions were normalized to the untreated cells (100 %) and the curve fitted using semilog dose-response curve in GraphPad Prism. The EC_{50} value is expressed as the mean ± SEM of three independent experiments.

The cell viability of compounds SRT5 and SRT6 was also determined by pre-incubating with an anti-CD44 antibody (IM7, eBioscience) for 30 min at rt. This was conducted after the 24 h incubation period and prior to replacing the wells with fresh media containing target compounds (0.01–100 μM). The plates were then incubated for 5 days.

4.2.5. HA-FITC binding assay

Adherent MDA-MB-231 cells were trypsinized, counted, and diluted in DMEM in order to have 5×10^4 cells/eppendorf tube. Cells were centrifuged for 5 min, and pellets were resuspended in DMEM media containing **SRT1**, **SRT5** or **SRT6** (120 μg/mL). Samples were incubated at 4 °C for 30 min. Then, cells were centrifuged for 5 min, and pellets were resuspended in DMEM media containing HA-FITC (20 μg/mL) and incubated at 4 °C for 15 min. Cells incubated with unlabelled HA were used as the negative control, whereas cells incubated with HA-FITC served as the positive control. After incubation, cells were centrifuged and resuspended in PBS, and samples were analyzed by flow cytometry (FACSCanto II). Flowjo® 10 software was used for data analysis. Results are expressed as the MFI ±SD of three independent experiments.

4.2.6. Cell viability assay in the presence of anti-CD44 antibody

MDA-MB-231 (2000 cells/well) were seeded in a 96-well plate format and incubated for 24 h. Each well was then replaced with fresh media, containing anti-CD44 antibody (IM7, eBioscience) and incubated for 30 min. The wells were replaced with fresh media containing target compounds at the IC_{50} concentration and incubated for 5 days. Untreated cells and cells treated with IM7 were used as controls. Each experiment was performed in triplicates. PrestoBlue™ cell viability reagent (10 % *v/v*) was added to each well and the plate incubated for 120 min. Fluorescence emission was detected using a GloMax-Multi Detection System (excitation filter at 540 nm and emission filter at 590 nm). The cell viability % is expressed as the mean ± SD of three independent experiments.

4.2.7. Apoptosis studies

NCl–H23 cells were seeded at 5×10^4 cells/well in a 24-well plate. After 24 h, cells were treated with **SRT1, SRT5 and SRT6** 10 μM for 48h. Cells incubated in the absence of the apoptosis inducing agent were used as the negative control, whereas cells incubated with H_2O_2 (5 mM) for 3 h at 37 °C served as the positive control. The experiments were performed using the Annexin V-FITC detection kit (Tali Apoptosis Kit -Annexin V Alexa Fluor 488 and propidium iodide (A10788, Invitrogen Europe Limited, Renfrew, UK)) according to the manufacturer's instructions, and the samples were analyzed by flow cytometry with a FACSCanto II flow cytometer. Flowjo® 10 software was used for data treatment. The analysis was performed in three independent assays.

4.2.8. Statistical analysis

Statistical analysis of experiments were carried out with one-way ANOVA analysis and Student's t-test except for apoptosis studies, which were performed using two-way ANOVA followed by Dunnett's multiple comparison test, using GraphPad Prism 8.0 software.

4.2.9. Kinase inhibition assays

The kinase inhibition profile of compounds **SRT1**, **SRT5** and **SRT6** was defined using a panel of 31 protein kinases and 2 lipid kinases. Residual activity values were measured by testing each compound at two concentrations (5 and 50 μM) for each kinase assay. Detailed methods for kinome analyses are given in the Supplementary data.

4.3. Computational studies

The murine CD44-HABD crystal structure (PDB ID: 5BZK) at 1.4 Å resolution [15] was used to perform the computational analysis. The binding mode of the compounds were explored through docking, followed by molecular dynamics (MD) simulations for select docking poses. Ligand structures were initially built using GaussView6 and subsequently optimised. The optimization process was conducted first at the Hartree-Fock level with a 6-31G(d,p) basis set, followed by refinement using the B3LYP functional with the same basis set.

Docking simulations were carried out using the CB-Dock2 server [31],[32] with default settings to target five cavities. Protein and ligand files were processed via a Perl script, employing AutoDock Vina version 1.2.0 for unbiased docking and BioLip database templates for template-guided docking (https://zhanggroup.org/BioLiP/index.cgi). Optimal ligand conformations were selected based on docking scores, energy parameters, and visual inspection.

MD simulations were performed using NAMD2.14 [33] with the CHARMM 36 force field for proteins and ions [34],[35], and the TIP3P model for water [36]. Ligand parameters and charges were obtained through the CHARMM-GUI ligand modeller interface [37], leveraging the CHARMM library or CHARMM General Force Field (CGenFF). Parameter evaluations conducted via the ParamChem server revealed no need for further adjustments. Each simulation system was embedded in a water box ($90 \times 90 \times 90$ Å^3) with KCl at a 150 mM concentration, resulting in approximately 45,000 atoms per system. Five independent replicas, each lasting 200 ns, were generated for a cumulative trajectory time of 7 μs after equilibration. Equilibration steps included 10,000 energy minimization iterations followed by 10 ns of constant temperature and constant pressure (NPT) dynamics, with a 1-fs timestep, and 200 ns of unrestricted NPT dynamics, also with a 1- fs timestep. Restraints on heavy atoms of proteins and ligands were gradually decreased over four 50 ps intervals: proteins and ligands from 1.0 to 0.1 kcal/mol for backbones and 0.5 to 0.05 kcal/mol for sidechains.

Electrostatic interactions were computed via the Particle Mesh Ewald method using a grid spacing of 1.0 Å [38] and NAMD's default spline and κ values. Non-bonded interactions employed a cutoff distance of 12 Å, with smooth switching from 10 Å. The Verlet-I/r-RESPA algorithm [39] was used for motion integration. Temperature was controlled at 298 K using a Langevin thermostat with damping coefficient 1 ps^{-1} [40]. Pressure was stabilized at 1 atm *via* a Langevin piston with damping constant 25 ps and a period of 50 ps [41]. Analysis of simulation trajectories was conducted using VMD software and custom Tcl scripts [42].

CRediT authorship contribution statement

Soledad Romero-Tamudo: Methodology, Investigation, Formal analysis, Data curation. **M. Dora Carrión:** Writing – original draft, Supervision, Methodology, Investigation, Formal analysis, Conceptualization, Data curation, Project administration, Validation, Writing – review & editing. **Meriem Chayah:** Writing – review & editing, Writing – original draft, Methodology, Investigation, Formal analysis, Data curation, Conceptualization. **Jose M. Espejo-Román:** Methodology, Investigation, Data curation. **Carmen Domene:** Writing – review & editing, Writing – original draft, Validation, Supervision, Funding acquisition, Formal analysis. **Rosario M. Sánchez-Martín:** Validation, Supervision. **Olga Cruz-López:** Writing – review & editing, Writing – original draft, Validation, Supervision, Project administration, Funding acquisition, Formal analysis, Conceptualization. **Ana Conejo-García:** Writing – review & editing, Writing – original draft, Validation, Supervision, Project administration, Funding acquisition, Formal analysis, Conceptualization.

Declaration of generative AI and AI-assisted technologies in the writing process

During the preparation of this work the authors used Microsoft Copilot in order to improve the readability of the manuscript. After using this service, the authors reviewed and edited the content as needed and take full responsibility for the content of the published article.

Declaration of competing interest

The authors declare that they have no known competing financial interests or personal relationships that could have appeared to influence the work reported in this paper.

Acknowledgment

This work was funded by the project PID2021.128109OB.I00 financed by MICIU/AEI/10.13039/501100011033. C.D. thanks computing time awarded on the UK Tier 2 systems JADE and Bede, provided via the UK High-End Computing Consortium for Biomolecular Simulation (HECBioSim, http://hecbiosim.ac.uk) and supported by EPSRC (grant no. EP/R029407/1), as well as on the Red Española de Supercomputación.

For the purpose of open access, C.D. has applied a Creative Commons Attribution (CC BY) license to any Author Accepted Manuscript version arising from this submission.

Funding for open access charge: Universidad de Granada/CBUA.

Appendix A. Supplementary data

Supplementary data to this article can be found online at https://doi.org/10.1016/j.ejmech.2025.118039.

Data availability

Data will be made available on request.

References

[1] F. Bray, M. Laversanne, H. Sung, J. Ferlay, R.L. Siegel, I. Soerjomataram, A. Jemal, Global cancer statistics 2022: GLOBOCAN estimates of incidence and mortality worldwide for 36 cancers in 185 countries, CA Cancer J. Clin. 74 (2024) 229–263, https://doi.org/10.3322/caac.21834.

[2] L. Zhou, D. Sheng, Q. Deng, D. Wang, S. Liu, Development of a novel method for rapid cloning of shRNA vectors, which successfully knocked down CD44 in mesenchymal triple-negative breast cancer cells, Cancer Commun. 38 (2018) 57, https://doi.org/10.1186/s40880-018-0327-7.

[3] Q. Huang, L. Liu, D. Xiao, Z. Huang, W. Wang, K. Zhai, X. Fang, J. Kim, J. Liu, W. Liang, J. He, S. Bao, CD44+ lung cancer stem cell-derived pericyte-like cells cause brain metastases through GPR124-enhanced trans-endothelial migration, Cancer Cell 41 (2023) 1621–1636.e8, https://doi.org/10.1016/j.ccell.2023.07.012.

[4] B.P. Toole, Hyaluronan-CD44 interactions in cancer: paradoxes and possibilities, Clin. Cancer Res. 15 (2009) 7462–7468, https://doi.org/10.1158/1078-0432.CCR-09-0479.

[5] Z. Yaghobi, A. Movassaghpour, M. Talebi, M. Abdoli Shadbad, K. Hajiasgharzadeh, S. Pourvahdani, B. Baradaran, The role of CD44 in cancer chemoresistance: a concise review, Eur. J. Pharmacol. 903 (2021) 174147, https://doi.org/10.1016/j.ejphar.2021.174147.

[6] L. Arabi, A. Badiee, F. Mosaffa, M.R. Jaafari, Targeting CD44 expressing cancer cells with anti-CD44 monoclonal antibody improves cellular uptake and antitumor efficacy of liposomal doxorubicin, J. Control. Release 220 (2015) 275–286, https://doi.org/10.1016/j.jconrel.2015.10.044.

[7] S. Zhang, C.C. Wu, J.F. Fecteau, B. Cui, L. Chen, L. Zhang, R. Wu, L. Rassenti, F. Lao, S. Weigand, J.K. Thomas, Targeting chronic lymphocytic leukemia cells with a humanized monoclonal antibody specific for CD44, Proc. Natl. Acad. Sci. USA 110 (2013) 6127–6132, https://doi.org/10.1073/pnas.1221841110.

[8] Y. Hirota-takahata, H. Harada, I. Tanaka, T. Nakata, M. Nakajima, M. Takahashi, F-16438s, novel binding inhibitors of CD44 and hyaluronic acid. I. Establishment of an assay method and biological activity, J. Antibiot. 59 (2006) 777–784, https://doi.org/10.1038/ja.2006.102.

[9] Y. Hirota-takahata, H. Harada, I. Tanaka, T. Nakata, M. Nakajima, M. Takahashi, F-19848 A, a novel inhibitor of hyaluronic acid binding to cellular receptor CD44, J. Antibiot. 60 (2007) 633–639, https://doi.org/10.1038/ja.2007.81.

[10] B.P. Toole, S. Ghatak, S. Misra, Hyaluronan oligosaccharides as a potential anticancer therapeutic, Curr. Pharm. Biotech. 9 (2008) 249–252, https://doi.org/10.2174/138920108785161569.

[11] M.G. Slomiany, L. Dai, L.B. Tolliver, G.D. Grass, Y. Zeng, B.P. Toole, Inhibition of functional hyaluronan-CD44 interactions in CD133-positive primary human ovarian carcinoma cells by small hyaluronan oligosaccharides, Clin. Cancer Res. 15 (2009) 7593–7601, https://doi.org/10.1158/1078-0432.CCR-09-2317.

[12] X. Lu, X. Huang, Design and syntheses of hyaluronan oligosaccharide conjugates as inhibitors of CD44-Hyaluronan binding, Glycoconj. J. 32 (2015) 549–556, https://doi.org/10.1007/s10719-015-9597-3.

[13] S. Banerji, A. Wright, M. Noble, D.J. Mahoney, I.D. Campbell, A.J. Day, D. G. Jackson, Structures of the CD44–hyaluronan complex provide insight into a fundamental carbohydrate-protein interaction, Nat. Struct. Mol. Biol. 14 (2007) 234–239, https://doi.org/10.1038/nsmb1201.

[14] M. Takeda, S. Ogino, R. Umemoto, M. Sakakura, M. Kajiwara, K.N. Sugahara, H. Hayasaka, M. Miyasaka, H. Terasawa, I. Shimada, Ligand-induced structural changes of the CD44 hyaluronan-binding domain revealed by NMR, J. Biol. Chem. 281 (2006) 40089–40095, https://doi.org/10.1074/jbc.M608425200.

[15] L.-K. Liu, B.C. Finzel, Fragment-based identification of an inducible binding site on cell surface receptor CD44 for the design of protein–carbohydrate interaction inhibitors, J. Med. Chem. 57 (2014) 2714–2725, https://doi.org/10.1021/jm5000276.

[16] J.M. Espejo-Román, B. Rubio-Ruiz, V. Cano-Cortés, O. Cruz-López, S. Gonzalez-Resines, C. Domene, A. Conejo-García, R.M. Sánchez-Martín, Selective anticancer therapy based on a HA-CD44 interaction inhibitor loaded on polymeric nanoparticles, Pharmaceutics 14 (2022) 788, https://doi.org/10.3390/pharmaceutics14040788.

[17] J.M. Espejo-Román, B. Rubio-Ruiz, M. Chayah-Ghaddab, C. Vega-Gutierrez, G. García-García, A. Muguruza-Montero, C. Domene, R.M. Sánchez-Martín, O. Cruz-López, A. Conejo-García, N-aryltetrahydroisoquinoline derivatives as HA-CD44 interaction inhibitors: design, synthesis, computational studies, and antitumor effect, Eur. J. Med. Chem. 258 (2023) 115570, https://doi.org/10.1016/j.ejmech.2023.115570.

[18] M. Chayah-Ghaddab, J.M. Espejo-Román, L. Erviti-Marticorena, F. Huertas-Camarasa, C. Domene, R.M. Sánchez-Martín, A. Conejo-García, O. Cruz-López, New N-Alkylketonetetrahydroisoquinoline derivatives exhibits antitumor effect by HA-CD44 interaction inhibition in MDA-MB-231 breast cancer, Biorg. Chem. 156 (2025) 108212, https://doi.org/10.1016/j.bioorg.2025.108212.

[19] J.M. Song, J. Im, R.S. Nho, Y.H. Han, P. Upadhyaya, F. Kassie, Hyaluronan-CD44/RHAMM interaction-dependent cell proliferation and survival in lung cancer cells, Mol. Carcinog. 58 (2019) 321–333, https://doi.org/10.1002/mc.22930.

[20] Y. Zhang, X. Chen, C. Gueydan, J. Han, Plasma membrane changes during programmed cell deaths, Cell Res. 28 (2018) 9–21, https://doi.org/10.1038/cr.2017.133.

[21] B.A. Carneiro, W.S. El-Deiry, Targeting apoptosis in cancer therapy, Nat. Rev. Clin. Oncol. 17 (2020) 395–417, https://doi.org/10.1038/s41571-020-0341-y.

[22] A. Conejo-García, Y. Jiménez-Martínez, R. Cámara, F. Franco-Montalbán, J. Peña-Martín, H. Boulaiz, M.D. Carrión, New substituted benzoxazine derivatives as potent inducers of membrane permeability and cell death, Bioorg. Med. Chem. 111 (2024) 117849, https://doi.org/10.1016/j.bmc.2024.117849.

[23] S. Kari, K. Subramanian, I.A. Altomonte, A. Murugesan, O. Yli-Harja, M. Kandhavelu, Programmed cell death detection methods: a systematic review and a categorical comparison, Apoptosis 27 (2022) 482–508, https://doi.org/10.1007/s10495-022-01735-y.

[24] S.A. Alshehade, H.A. Almoustafa, M.A. Alshawsh, Z. Chik, Flow cytometry-based quantitative analysis of cellular protein expression in apoptosis subpopulations: a protocol, Heliyon 10 (2024) e33665, https://doi.org/10.1016/j.heliyon.2024.e33665.

[25] C. Chen, S. Zhao, A. Karnad, J.W. Freeman, The biology and role of CD44 in cancer progression: therapeutic implications, J. Hematol. Oncol. 11 (2018) 64, https://doi.org/10.1186/s13045-018-0605-5.

[26] B. Geng, J. Pan, T. Zhao, et al., Chitinase 3-like 1-CD44 interaction promotes metastasis and epithelial-to-mesenchymal transition through β-catenin/Erk/Akt signaling in gastric cancer, J. Exp. Clin. Cancer Res. 37 (2018) 208, https://doi.org/10.1186/s13046-018-0876-2.
[27] C. Tomuleasa, A.B. Tigu, R. Munteanu, et al., Therapeutic advances of targeting receptor tyrosine kinases in cancer, Sig. Transduct, Target Ther 9 (2024) 201, https://doi.org/10.1038/s41392-024-01899-w.
[28] R.C. Bates, N.S. Edwards, G.F. Burns, D.E. Fisher, A CD44 survival pathway triggers chemoresistance via Lyn Kinase and phosphoinositide 3-Kinase/Akt in Colon carcinoma cells, Cancer Res. 61 (2001) 5275–5283.
[29] A.B. Gurung, A. Bhattacharjee, M.A. Ali, Exploring the physicochemical profile and the binding patterns of selected novel anticancer Himalayan plant derived active compounds with macromolecular targets, Inform. Med. Unlocked 5 (2016) 1–14, https://doi.org/10.1016/j.imu.2016.09.004.
[30] Y. Fukunishi, H. Nakamura, Definition of drug-likeness for compound affinity, J. Chem. Inf. Model. 51 (2011) 1012–1016, https://doi.org/10.1021/ci200035q.
[31] Y. Liu, X. Yang, J. Gan, S. Chen, Z.-X. Xiao, Y. Cao, CB-Dock2: improved protein-ligand blind docking by integrating cavity detection, docking and homologous template fitting, Nucleic Acids Res. 50 (2022) W159–W164, https://doi.org/10.1093/nar/gkac394.
[32] X. Yang, Y. Liu, J. Gan, Z.-X. Xiao, Y. Cao, FitDock: protein-ligand docking by template fitting, Brief Bioinform 23 (2022) 1–11, https://doi.org/10.1093/bib/bbac087.
[33] J.C. Phillips, D.J. Hardy, J.D.C. Maia, J.E. Stone, J.V. Ribeiro, R.C. Bernardi, R. Buch, G. Fiorin, J. Henin, W. Jiang, R. McGreevy, M.C.R. Melo, B.K. Radak, R. D. Skeel, A. Singharoy, Y. Wang, B. Roux, A. Aksimentiev, Z. Luthey-Schulten, L. V. Kale, K. Schulten, C. Chipot, E. Tajkhorshid, Scalable molecular dynamics on CPU and GPU architectures with NAMD, J. Chem. Phys. 153 (2020) 044130, https://doi.org/10.1063/5.0014475.
[34] J. Huang, A.D. MacKerell, CHARMM36 all-atom additive protein force field: validation based on comparison to NMR data, J. Comput. Chem. 34 (2013) 2135–2145, https://doi.org/10.1002/jcc.23354.
[35] A.D. MacKerell, D. Bashford, M. Bellott, R.L. Dunbrack, J.D. Evanseck, M.J. Field, S. Fischer, J. Gao, H. Guo, S. Ha, D. Joseph-McCarthy, L. Kuchnir, K. Kuczera, F.T. K. Lau, C. Mattos, S. Michnick, T. Ngo, D.T. Nguyen, B. Prodhom, W.E. Reiher, B. Roux, M. Schlenkrich, J.C. Smith, R. Stote, J. Straub, M. Watanabe, J. Wiórkiewicz-Kuczera, D. Yin, M. Karplus, All-atom empirical potential for molecular modeling and dynamics studies of proteins, J. Phys. Chem. B 102 (1998) 3586–3616, https://doi.org/10.1021/jp973084f.
[36] W.L. Jorgensen, J. Chandrasekhar, J.D. Madura, R.W. Impey, M.L. Klein, Comparison of simple potential functions for simulating liquid water, J. Chem. Phys. 79 (1983) 926–935, https://doi.org/10.1063/1.445869.
[37] S. Kim, J. Lee, S. Jo, C.L. Brooks III, H.S. Lee, W. Im, CHARMM-GUI ligand reader and modeler for CHARMM force field generation of small molecules, J. Comput. Chem. 38 (2017) 1879–1886, https://doi.org/10.1002/jcc.24829.
[38] T. Darden, D. York, L. Pedersen, Particle mesh Ewald: an N·log(N) method formEwald sums in large systems, J. Chem. Phys. 98 (1993) 10089–10092, https://doi.org/10.1063/1.464397.
[39] L. Verlet, Computer “experiments” on classical fluids. I. Thermodynamical properties of Lennard-Jones molecules, Phys. Rev. 159 (1967) 98–103, https://doi.org/10.1103/PhysRev.159.98.
[40] E.A. Koopman, C.P. Lowe, Advantages of a Lowe-Andersen thermostat in molecular dynamics simulations, J. Chem. Phys. 124 (2006) 204103, https://doi.org/10.1063/1.2198824.
[41] S.E. Feller, Y. Zhang, R.W. Pastor, B.R. Brooks, Constant pressure molecular dynamics simulation: the Langevin piston method, J. Chem. Phys. 103 (1995) 4613–4621, https://doi.org/10.1063/1.470648.
[42] W. Humphrey, A. Dalke, K. Schulten, VMD: visual molecular dynamics, J. Mol. Graph. 14 (1996) 33–38, https://doi.org/10.1016/0263-7855(96)00018-5.